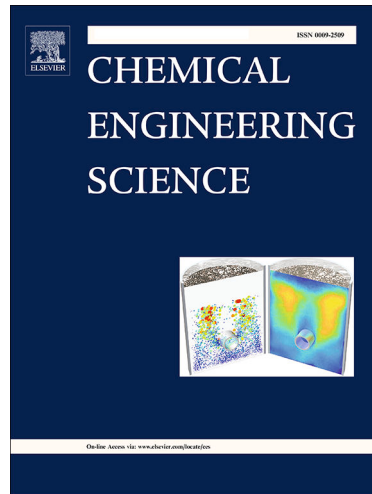


Journal Pre-proofs

Numerical analysis of pre-dryout sequences through the route of interfacial evolution in annular gas-liquid two-phase flow with phase change

Liril D. Silvi, Avik Saha, Dinesh K. Chandraker, Sumana Ghosh, Arup K. Das

PII: S0009-2509(19)30846-2
DOI: <https://doi.org/10.1016/j.ces.2019.115356>
Reference: CES 115356



To appear in: *Chemical Engineering Science*

Received Date: 5 September 2019
Revised Date: 8 November 2019
Accepted Date: 15 November 2019

Please cite this article as: L.D. Silvi, A. Saha, D.K. Chandraker, S. Ghosh, A.K. Das, Numerical analysis of pre-dryout sequences through the route of interfacial evolution in annular gas-liquid two-phase flow with phase change, *Chemical Engineering Science* (2019), doi: <https://doi.org/10.1016/j.ces.2019.115356>

This is a PDF file of an article that has undergone enhancements after acceptance, such as the addition of a cover page and metadata, and formatting for readability, but it is not yet the definitive version of record. This version will undergo additional copyediting, typesetting and review before it is published in its final form, but we are providing this version to give early visibility of the article. Please note that, during the production process, errors may be discovered which could affect the content, and all legal disclaimers that apply to the journal pertain.

Numerical analysis of pre-dryout sequences through the route of interfacial evolution in annular gas-liquid two-phase flow with phase change

Liril D. Silvi¹, Avik Saha², Dinesh K. Chandraker³, Sumana Ghosh^{1*}, Arup K Das²

¹Department of Chemical Engineering, Indian Institute of Technology, Roorkee

²Department of Mechanical Engineering, Indian Institute of Technology, Roorkee

³Reactor Engineering Division, Bhabha Atomic Research Centre, Mumbai

*Corresponding author Email: ghoshfch@iitr.ac.in

Abstract

Numerical modeling of two-phase annular flow boiling has been carried out inside a tube using volume of fluid based computational multifluid dynamics. The proposed numerical methodology has been validated with available experimental results from literature. The stages of bubble nucleation, growth, merging, bursting, droplet entrainment, film rewetting, and dryout has been clearly visualized for diabatic annular mist flow. Plots of liquid phase fraction and average heat transfer coefficient were plotted which shows decreasing trends with axial space. Effect of different degrees of superheats and gas-liquid velocities at a higher working pressure of 40 bar have been studied, which can be commonly be observed in boiling water reactor (BWR) conditions. Dryout is found to happen early in the axial length if the degree of superheat and flow velocities increases. The chaotic interfacial behavior has been analyzed with mean, standard deviation and attractor plot of space time-varying values of liquid phase fraction.

Keywords: Annular flow, Boiling, Merging, Bubble, Bursting, Rewetting, Two-phase flow, Dryout, Nucleation

1. Introduction

Gas-liquid two-phase flows with phase change, which is popularly known as flow boiling, has a wide range of applications in refrigeration, power, chemical, and nuclear power plant having industrial components like evaporators, boilers, distillation towers, steam generators and many more. Among different flow boiling configurations, vertically upward flow is widely used because it allows easy escape of the vapor due to the buoyancy effect. Depending upon interfacial deformations, relative velocities, varying pressure, and wall heat flux conditions inside the pipeline during upward flow boiling, different flow patterns have been observed by researchers over the years. Collier and Thome (1994), has identified and categorized different sections of the vertical flow boiling into flow regime such as subcooled, nucleate boiling, bubbly, slug, annular and mist flow. To understand the higher limit of flow boiling one should study annular and mist flow in detail. Annular flow can be recognized when

the liquid is present at the periphery of the tube with gas flow at the core. On the other hand, mist flow will only have the identity of upward-moving drop flow throughout the tube. At the end of the annular flow regime, the liquid film at the wall extinct due to a combined effect of shearing caused by core vapor and sustained film boiling due to continuous heat addition from the wall. This is commonly referred to as the onset of dryout in the literature (Collier and Thome, 1994). Due to the interaction of interfacial waves and bubble bursting, liquid entrainment happens in the vapor core of annular flow and the scattered droplet flow regime starts, which is also called as liquid deficient region or mist flow zone (Collier and Thome, 1994). In mist flow region, the heat is transferred from the wall to the liquid drops via convection from superheated vapor or by direct conduction during its impingement on the hot wall. This leads to complete conversion of liquid droplets into vapor and beyond this mist regime, single-phase vapor flow starts, which is called a complete dryout condition (Andreani and Yadigaroglu, 1994). In post dryout conditions, the heat transfer reduces drastically due to the low conductivity of the vapor and wall temperature rises sharply which can damage and even deform the tube wall. This may lead to a hazardous situation in industrial applications like a boiler in a powerplant. It can even turn into nuclear hazards due to leakage of radioactive substances in case of a nuclear boiler. Hence, the prediction of dryout occurrence and post-dryout heat transfer conditions are crucial in the optimization of the design and operation of thermal equipment. In industries, empirical relations developed based on experiments are being used to predict dryout in flow boiling conditions (Tong, 2018). 1-D theoretical models such as FIDAS (Sugawara & Miyamoto, 1990, Sugawara et al., 1991), MONA-3 (Hoyer, 1998), COBRA-TF (Glück M, 2007), CATHARE-3 (Emonot et al., 2011, Velette et al., 2011), and VIPRE-W (Adamsson and Corre, 2011) are popular for dryout prediction with incorporation of three fields, the vapor, the liquid film and the droplets separately. For annular flow, total energy theory has been explored previously (El-Genk and Saber, 2001) to predict the minimum film thickness, however, it is not valid in case of annular mist flow. But these empirical models do not take care of the hydrodynamics of the liquid-gas flow directly and do not explore heat transfer mechanism from the fundamental principle of phase change.

Very few studies have been reported previously by researchers to shed light on the visualization of the dryout mechanism in flow boiling situation. Ishii and Denten (1990) studied the hydrodynamics of post-dryout flow characteristics and theoretically modeled annular-mist flow to calculate the liquid film flow based on the droplet entrainment, deposition, and vapor evaporation rate. Barbosa et al. (2003) visualized annular flow boiling through a transparent tube keeping the heater surface inside. They came up with an interesting observation of hot spots below highly turbulent disturbance wave and concluded that the disturbance wave to be responsible for triggering of nucleation beneath the annular thin film. CFD approach in the initial stage was used for simulation of multidimensional two-phase flow boiling in annular regime in the '90s (Jayanti and Hewitt, 1997, Anglart et al., 1997). Later on, a model of annular flow with the evaporating liquid film was developed based on Eulerian-Eulerian (Li

and Anglart, 2016A) and Eulerian-Lagrangian (Li and Anglart, 2016B) approach, aiming to predict the dryout occurrences. Recently, different modes of entrainment in adiabatic annular mist flow are identified by Kumar et al. (2016) using numerical study. The formation of disturbance wave and heat transfer in annular flow was also investigated by Yang et al. (2017) using advanced CFD tool TransAT with incorporation of level-set interface tracking method and large eddy simulation technique. It can be noted that theoretical and numerical modeling is gaining popularity in the prediction of dryout in flow boiling situations in industries.

Although numerous experimental studies have been performed to understand the mechanism that leads to dryout conditions in the flow boiling situation, due to metallic casing of pipe, interfacial dynamics of the flow boiling in annular regime is still not well understood. Till date, the numerical effort also has not been made to capture the dryout mechanism beneath annular flow. Seeing these voids in literature, in the present study, an effort has been made to numerically model vertically upward flow boiling situation and investigate the route to dryout inside a cylindrical tube. In present work, the effect of different operating parameters such as the degrees of superheat at tube wall and liquid-vapor velocities has been studied with the help of VOF based OpenFOAM numerical solver for phase change (Samkhaniani and Ansari, 2017). In the next section, the mathematical model of the solver has been discussed and subsequently domain description has been demonstrated, before the discussion of observed interface dynamics.

Nomenclature

A_D	The diagonal entries of the coefficient matrix of the momentum equation	V	Volume of individual cell
a	Thermal diffusivity	h	Enthalpy
C_α	Compression factor	\dot{V}''	Volume flux
D	Tube diameter	y	Thermal properties
\vec{g}	Gravitational acceleration	ΔT	Degree of superheat
k	Thermal conductivity	T_w	Wall temperature
d	Bubble diameter	Greek Letters	
\dot{m}'''	Volumetric rate of phase change (+ve for condensation and -ve for boiling)	α_L	Liquid phase fraction
M	Molecular Weight	β_L	Non-dimensionalized liquid phase fraction
P	Local pressure	κ	Interface curvature
t	Time	ρ	Density
C	Specific heat	σ	Surface tension
H_{LG}	Latent heat	μ	Viscosity
R	Universal gas constant	γ	Tanasawa coefficient
T	Temperature field	Subscript	
\vec{U}	Velocity field	L	Liquid
u	Inflow velocity	G	Gas
		sat	Saturation

2. Computational methodology

2.1. Mathematical model

Similar to any other multiphase flow simulation, in boiling heat transfer of annular flow, capturing the space and time-varying interface is the most crucial part. In the present study, the volume of fluid (VOF) based methodology has been adopted for the same. Here, one set of conservation equation is solved for both the phases. The thermo-physical properties (y) for both the phases can be calculated with Eq. (2). The liquid phase fraction and thermos-physical properties are related as:

$$\alpha_L(\vec{x},t) = \frac{V_L}{V} \quad (1)$$

$$y = \alpha_L y_L + (1.0 - \alpha_L) y_G \quad (2)$$

All the thermophysical properties (y) including density (ρ), conductivity (k), viscosity (μ) and specific heat (C) are calculated using similar (1-2) equations. The global continuity equation can be written as:

$$\frac{\partial}{\partial t}(\rho) + \nabla \cdot (\rho \vec{U}) = 0 \quad (3)$$

After placing the density (ρ) from Eq. (2) in Eq. (3) the following equation can be obtained:

$$\frac{\partial \alpha_L}{\partial t} + \vec{U} \cdot \nabla \alpha_L + \alpha_L \nabla \cdot \vec{U} = - \frac{\rho_G \nabla \cdot \vec{U}}{(\rho_L - \rho_G)} \quad (4)$$

In the case of incompressible adiabatic two-phase flow, the continuity equation can be written as $\nabla \cdot \vec{U} = 0$. Whereas, in phase change process, the local continuity equation for liquid and vapor phase can be written as:

$$\frac{\partial}{\partial t}(\rho_L) + \nabla \cdot (\rho_L \vec{U}) = - \dot{m}'' \quad (5)$$

$$\frac{\partial}{\partial t}(\rho_G) + \nabla \cdot (\rho_G \vec{U}) = + \dot{m}'' \quad (6)$$

As both phases are incompressible, the first term on the left hand of Eq. (5) and (6) is zero. The summation of the above two equations can be now converted to the following equation using the integral approach and divergence theorem (Samkhaniani and Ansari, 2017):

$$\nabla \cdot \vec{U} = \dot{m}''' \left(\frac{1}{\rho_G} - \frac{1}{\rho_L} \right) \quad (7)$$

Eq. (7) is be placed in Eq. (3) and the following transport equation is derived:

$$\frac{\partial \alpha_L}{\partial t} + \vec{U} \cdot \nabla \alpha_L = -\dot{m}''' \left[\frac{1}{\rho_L} - \alpha_L \left(\frac{1}{\rho_L} - \frac{1}{\rho_G} \right) \right] \quad (8)$$

In OpenFoam, an extra divergence term is added to avoid smearing of the interface (Klostermann et al, 2013). This term is applicable only in the interface region ($0 < \alpha_L < 1.0$):

$$\frac{\partial \alpha_L}{\partial t} + \vec{U} \cdot \nabla \alpha_L + \nabla \cdot (\alpha_L (1 - \alpha_L) \vec{U}_C) = -\dot{m}''' \left[\frac{1}{\rho_L} - \alpha_L \left(\frac{1}{\rho_L} - \frac{1}{\rho_G} \right) \right] \quad (9)$$

In the above equation, a source term has been added at the right-hand side to take care of the mass transfer (\dot{m}''') due to phase change. For evaluation of volumetric mass transfer rate \dot{m}''' ($\text{kg/m}^3\text{s}$), the following equation has been utilized as proposed by Tanasawa (1991). The constant γ is taken to be equal to 1 for film flow boiling as recommended by Marek and Straub (2001).

$$\dot{m}''' = \frac{2\gamma}{2 - \gamma} \sqrt{\frac{M \rho_G H_{LG} (T - T_{sat})}{2\pi R T_{sat}^{3/2}}} |\nabla \alpha_L| \quad (10)$$

Compressive velocity (\vec{U}_C) has been incorporated in the transport equation (Eq. 9) of phase fraction to avoid the dispersion of the two-phase interface due to source term as suggested by Albadawi et al. (2013). \vec{U}_C has been calculated from the following expression:

$$\vec{U}_C = \min \{C_\alpha |U|, \max |U|\} \frac{\nabla \alpha_L}{|\nabla \alpha_L|} \quad (11)$$

To capture the flow of the two-phases, the momentum equation can be written as:

$$\frac{\partial(\rho \vec{U})}{\partial t} + \nabla \cdot (\rho \vec{U} \vec{U}) - \nabla \cdot (\mu (\nabla \vec{U}^T + \nabla \vec{U})) = -\nabla P + \rho \vec{g} + \sigma \kappa \nabla \alpha_L \quad (12)$$

In the momentum equation, the last term corresponds to the surface tension force, which is modeled with the help of the continuum surface force model (Brackbill et al., 1992). It becomes non-zero only at the interfaces where the spatial variation of α_L exists. For calculation of the curvature (κ) following equation is used:

$$\kappa = -\nabla \cdot \left(\frac{\nabla \tilde{\alpha}_L}{|\nabla \tilde{\alpha}_L|} \right) \quad (13)$$

Here $\tilde{\alpha}_L$ is the smoothed value of α_L , among neighbors which helps in suppressing the spurious current generated due to sharp change of interface. In the present study, the smoother given by Lafaurie et al. (1994) has been used.

The energy conservation equation for the phase change process can be written as:

$$\frac{\partial}{\partial t}(\rho C_p T) + \nabla \cdot (\rho C_p U T) - \nabla \cdot (k \nabla T) = -\dot{m}''' H_{LG} \quad (14)$$

Where, H_{LG} represents the latent heat. The right-hand side term in the above equation calculates the heat transfer occurring while the phase change process. To calculate the mass flux rate (\dot{m}'''), Tanasawa (1991) mass transfer model has been used in the current simulation.

The small variations of saturation temperature with respect to the associated local pressure P has been considered and can be calculated by a simplified Clausius-Clapeyron equation:

$$\ln \frac{P_{sat,1}}{P_{sat,0}} = -\frac{MH_{LG}}{R} \left(\frac{1}{T_{sat,1}} - \frac{1}{T_{sat,0}} \right) \quad (15)$$

Local modelling of evaporation through microlayer has not been targeted in the present study, as the prime objective is to understand macroscopic bubble behaviour and its interaction with film. The initial microlayer thickness observed beneath the nucleating bubble is in the range of 0-9 μm for the case of pool boiling of water (Utaka et al., 2013). Such a micrometer level of film thickness can be captured with very fine meshing size, for which immense computational resources are required. Mukharjee and Dhir (2004), Sato and Niceno (2015) and Pandey et al. (2018) have incorporated microlayer model within their numerical model developed for the simulation of nucleate pool boiling around a single bubble. Evaporation of microlayer affects the heat transfer during nucleation, growth and departure of vapor bubble in pool boiling (Chi-Liang and Mesler, 1977; Utaka et al., 2013). But, the effect of microlayer makes negligible direct contribution to the heat flux for flow boiling (Del Valle and Kenning, 1985). On the other hand, its significance on bubble dynamics during high quality and high inertia driven flow boiling cases has been not well documented in literature. Keeping the same in mind and to reduce the computational effort, microlayer model has not been incorporated in the present mathematical model. Moreover, it is evident that if the disjoining pressure exceeds a critical value, evaporation in the microlayer gets suppressed. The calculation of mass transfer due to phase change based on Tanasawa's model depends on the value of saturation temperature. The small variation in saturation temperature as a function of the local pressure has been calculated with incorporation of modified Clausius-Clapeyron equation (Li and Dhir, 2007; Samkhaniani and Ansari, 2017). This gives macroscopic approximation of boiling through microscopic liquid layers

The algorithm of the solver describing the mathematical model step by step can be summarized as follows:

- i. Mesh initialization and setting up the internal field and boundary conditions.
- ii. Starting of the main loop with the calculation of time step Δt satisfying Courant-Friedrichs-Lowy condition (CFL number).

- iii. Solving the volume fraction equation using Eq. (9) with the MULES method (Multidimensional Universal Limiter with Explicit Solver) and all the properties such as μ , ρ , C and k for each cell are updated.
- iv. Enter into the PIMPLE loop. PIMPLE loop is a combination of PISO (Pressure Implicit with Splitting of Operators) and SIMPLE (Semi Implicit Method for Pressure Linked Equations) algorithms. It solves momentum Eq. (6) to guess velocity field and additional equation for pressure (Samkhaniani and Ansari, 2017) which is derived from continuity and momentum equation is solved.
- v. Eventually, the energy equation is solved using Eq. (14) to get the temperature field and mass transfer using Eq. (10) is calculated.
- vi. If the reported time is equal to the specified end time, then simulation stops. Otherwise, the loop restarts for the next iteration depending on the time step value Δt .

2.2. Discretization schemes and criterion for solution algorithm

The temporal term is discretized with Euler scheme, which is a first-order bounded implicit scheme. The divergence term in momentum and energy equation is discretized with vanLeerV and vanLeer schemes respectively (Van Leer, 1974). The extra divergence term added in momentum equation for incorporation of the compression velocity is discretized with interfaceCompression scheme developed by Weller (2008). The diffusion and viscous terms in momentum equation are discretized with Gauss Linear corrected and Gauss Linear schemes respectively, which are basically central difference schemes. The solution is considered to be converged if residual for velocity and pressure reaches 10^{-8} , whereas, temperature and phase fraction reaches 10^{-10} . The velocity of the fluids shows a drastic change in value; hence, adjustable time-stepping method has been used with the Courant Friedrichs Lewy (CFL) criterion taken equivalent to 0.25. With this CFL criteria, the time step value has been observed to be in the order of 10^{-6} .

2.3. Domain description:

For the simulation of annular flow boiling of water inside a tube, a representative cylindrical fluid domain of 11 mm diameter (D) and 50 mm length (L) has been chosen in the present study. A schematic of the domain along with necessary initial boundary conditions is shown in Figure 1 (a). Since in the majority of the industrial applications, boiling is performed at an elevated pressure above the atmospheric pressure, present simulations have been performed at a representative 40 bar of pressure (P_b). To mimic annular flow like situation, initially a thin 0.5 mm of the thermally saturated liquid film has been positioned at the outer periphery of the cylindrical domain and the rest core part is considered to be filled with saturated vapor at the corresponding pressure. No-slip and no penetration conditions have been applied to the cylindrical boundary of the domain. The contact angle at the heated wall is

considered to be 90° . Thermally the wall is considered to be maintaining ΔT_{wall} superheat above the saturation temperature of T_{sat} at P_b given in fluid domain. Other parameters like pressure and volume fraction are not supposed to have any gradient across the tube wall. Conditions at the wall can be summarized as:

$$\vec{U} = (0,0,0), \quad T = T_{sat} + \Delta T_{wall}, \quad \frac{\partial P}{\partial r} = \frac{\partial \alpha_L}{\partial r} = 0 \quad (15)$$

From the bottom of the domain, uniform and constant velocity inflow conditions have been applied which has split the inlet plane into two parts, consisting of one outer annular region, matching thickness liquid film inside (t), from where liquid enters and through rest of the inlet section vapor enters. Provisions have been kept for varying the average magnitude of inflow velocities for liquid and gas (u_g, u_l) independently.

Inflow boundary condition can be mathematically described as:

$$\vec{U} = \begin{cases} u_g & \text{for } r < \left(\frac{D}{2} - t\right) = 5 \text{ mm} \\ 0,0, & \\ u_l & \text{for } r \geq \left(\frac{D}{2} - t\right) = 5 \text{ mm} \end{cases}, \quad T = T_{sat},$$

$$\alpha_L = \begin{cases} 0 & \text{for } r < \left(\frac{D}{2} - t\right) = 5 \text{ mm} \\ 1 & \text{for } r \geq \left(\frac{D}{2} - t\right) = 5 \text{ mm} \end{cases} \quad (16)$$

The top boundary has been set as a pressure outlet with a constant value of P_b , signifying no axial flux of temperature, volume fraction and velocity. The same can be mathematically expressed as:

$$P_{@z=L} = P_b, \quad \frac{\partial T}{\partial z} = \frac{\partial \alpha_L}{\partial z} = \frac{\partial \vec{U}}{\partial z} = 0 \quad (17)$$

All the steam and liquid water properties are taken at (P_b, T_{sat}) . Representative values for the present simulation are shown in Table 1.

Table 1: Account of gas and liquid properties, fed in the code at $P_b = 40 \text{ bar}$ and T_{sat}

Property	Liquid	Vapour
Density (kg/m^3)	798.7	20
Thermal Conductivity (W/mK)	0.62	0.0513
Viscosity (m/s^2)	1.3521×10^{-7}	9×10^{-7}
Specific Heat (J/kgK)	4865	3795

Latent Heat (kJ/kg)	1714
Surface Tension(N/m)	0.02301
Gravity (m/s ²)	9.81

The mesh structure of the domain in a cross-sectional and longitudinal view can be observed in Figure 1 (b) and (c), respectively. Since boiling will occur near the wall only, a highly refined mesh has been generated near the wall to have a better understanding of bubble nucleation due to boiling. Enough care has also been taken to refine mesh near the interface. This can be clearly seen from the enlarged cross-sectional view, as shown in Figure 1 (d). The grid-independent study has been carried out for 3 different cases of grid sizes as shown in Table 2 and Figure 2. The plot of vapor volume present at steady state in the annular region over the time shows that there is a very small change in the trend between medium and fine mesh as compared to coarse mesh (see Figure 2 (b)). From the grid independency statistics (see Table 2) and contours, it is clear that coarse mesh is under-predicting the vapor generation rate with 3.5 % difference compared to medium mesh. Whereas finer mesh has shown only 0.3 % improvement in the result but at the same time it consumes immense computational effort. To shed light on assurance with grid independency, the interfacial dynamics of coarse, medium and fine mesh has been plotted as shown in Figure 2 (a) & (c). After the mentioned observations, the medium mesh was selected to carry out further simulations for different cases. For medium mesh type, smallest cell size is $\Delta x = 0.03$ mm which can accurately capture liquid film having thickness larger than Δx . At the same time in our study at least 4 cells are required to capture isolated gaseous entity as bubble. Hence, smallest bubble which the present simulation can capture is in the range of ~ 120 μm . Prediction capability of the model can be improved further by minimizing the mesh size. In present study, as we have restricted our discussion within bubbles dynamics and its implication on film, medium mesh type is sufficient for analysis.

Table 2. Grid independence test mesh statistics

Case	1-Coarse	2-Medium	3-Fine
Number of cells	1799864	3764926	6631248
Min. cell size (mm)	0.045	0.03	0.02
Run time for 2 ms (hr)	1.629	8.51	29.25
% improvement from coarser one	-	3.5	0.3

The simulations were performed for various liquid and vapor velocities as well as with different degrees of superheats. The present discussion will be only describing a few of these mentioned in Table 3, which will help in understanding the parametric effect on interfacial dynamics. It can be noted that

with described range of wall temperature, simulations will be restricted within nucleate boiling regime ($\sim 200 \text{ kW/m}^2$). Applied wall temperature can be increased further or constant heat flux boundary condition can be used for simulation of critical heat flux like situation in which bubble dynamics will be further chaotic. As in the present study, our major concern is to understand the elemental bubble behaviour and its interaction with film, wall temperature has been kept well below the limit of critical heat flux. Study of bubble behaviour at critical heat flux can be considered as future scope of present study.

Table 3: Description of simulation parameters for annular flow with phase change

Case	P_b in bar	(u_g, u_l) in m/s	ΔT_{wall} ($^{\circ}\text{C}$)
A	40	(2.5,1)	20
B			10
C		(3.4,1)	20
D			50
E		(4.5,1)	20
F		(10,1)	20
G		(15,1)	50
H		(3.4,1.5)	20

2.4. Validation:

As interfacial dynamics is not reported in the literature for annular flow boiling, for validation, boiling on a rectangular parallelepiped geometry, having similar mesh configuration as a cylinder, has been studied. The growth history of a bubble in terms of equivalent diameter is plotted in Figure 3 (a) over the time before it gets detached from the surface. The same has been compared with the simple but most fundamental and popular correlation of Plessset and Zwick (1954). Our simulation predicts the trend of growth rate quite well once the bubble takes nearly spherical shape and a maximum error of less than 2.7% has been noticed, before departure. Encouraging accuracy and observation ability of interfacial dynamics of the present model prompt confidence in modeling interface dynamics during flow boiling cases with cylindrical geometry. The results of the same are described in the next section.

After comparing the outcome of the evolution of the single spherical vapor bubble with Plessset-Zwick equation, a simulation was conducted for annular flow boiling conditions having similar flow and heating conditions as mentioned in the experiment conducted by Becker et al. (1983). From their experiments, case no. 334 having heat flux of 562 kW/m^2 , mass flux of $497 \text{ kg/m}^2\text{s}$ and pressure of 30 bar is simulated with the geometry as shown in Figure 1. The post dryout heat transfer parameters like wall temperature and enthalpy with different quality of steam has been calculated numerically. For a better comparison between numerical and experimental results, the ratio of temperature and enthalpy is

plotted as shown in Figure 3 (b). From this plot, it is evident that the maximum error is found out to be less than 10 %.

3. Results and discussion:

3.1. Interfacial dynamics representing vapor bubble evolution:

Observations of numerical simulation till initial 5 ms are analyzed in the form of interfacial phase fraction (VOF) contour for understanding the breaking and making the process of the interface as shown in Figure 4. Simulation parameters considering the degree of superheat of wall and account of velocity inlet are given in Table 3. As a representation, case G is described over here. The initial undisturbed film, at around 1 ms shows the initiation of the disturbance wave at axial length of 3 mm. At the same time due to the change of phase throughout the superheated wall, a thin vapor film generates which soon transforms into discrete nucleations throughout the axial length (~ 2 ms). Along with the growth of these bubbles, the disturbance wave continues to transform into a roll like lamella. Upon reaching specific overhung, due to surface tension and shearing action of the gas phase, lamellas shed droplets at ~ 3 ms (Kumar et al., 2016). These droplets inside the tube create a droplet swarm and convert the flow pattern to droplet annular one. For an adiabatic situation, the same has been already described by Kumar et al. 2016. In the presence of phase change, at the foothill of the disturbance wave, nucleating bubble bursts to form a local vapor patch which creates dryout like situations (~ 5 ms), commonly happening in annular flow with the heated wall. A close look at the interfacial nature of the bubbles generated due to phase change shows several stages in its life cycle. Distinctly, these stages can be identified as shown in Figure 5 as (i) nucleation (ii) growth (iii) merging with neighbors and (iv) bursting at the film-free surface. On the other hand, droplet pinches off at the gas-liquid interface as a result of excessive amplitude in the wave, can be observed in stage iv. The cumulative effect of generated bubble dynamics and the aftermath of pinch-off lead towards local dryout. The description of individual stages is given below.

Nucleation: At the beginning, a thin vapor film ($<50\mu\text{m}$) is formed at the wall by evaporating the saturated liquid adjacent to the superheated wall. Soon the film becomes asymmetric axially due to buoyancy and one can see several nucleation sites based on mutual interaction of buoyancy-driven flow and surface tension instability. These nucleating bubbles are in the size range of 0.5 mm which decreases in the radius of curvature as time progresses. Nucleation due to strong surface tension effect converts into a hemispherical bubble shape and climbs up before entering into the growth stage. The nucleation stage is shown as phase contour in-between 9 ms and 11 ms in Figure 5.

Bubble Growth: In this stage, liquid inertia drives the nucleated bubbles to advance in the upward direction and since constant wall temperature is applied over the wall, heat transfer will take place resulting in further growth of bubbles in size. This process continues until two neighboring bubbles

(preceding and succeeding) comes closer to each other and indulges in the mutual merging process as shown in Figure 5.

Bubble Merging: Due to the favorable difference of velocities in neighboring bubbles and their individual growth, lagging in front of preceding bubble and leading front of succeeding bubble come close to each other by draining the liquid in-between. After overcoming thin-film repulsive forces, these bubbles unify and reoriented its interface into a combined single bubble. This coalescence of bubbles results in a sudden increase in the vapor volume and size of the bubble.

Bubble Bursting: As an aftermath of the sudden increase in bubble size due to merging, the innermost point of the combined bubble may come closer to the wavy liquid film. In the case of lamella formation and pinch-off of the droplet due to the excessive amplitude of the wave, local ripping of film thickness can be observed at the foothill of the lamella. Incidentally, if the bubble merging happens at the foothill of the drop ejecting lamella then unified bubble may burst at the liquid-vapor interface. At around 15.8 ms of the present simulation, a similar situation can be observed where the merged bubble opens up in the central vapor core through bubble bursting. Such a procedure generates a local dryout patch, which further elongates in length due to the circulation of air inside the burst vapor cavity.

Droplet Pinch-off: Simultaneously, one can also observe droplet pinch-off from the inner wavy interface, which plays a major role in the transformation of annular flow to dryout situation through droplet annular regime. Figure 5 also shows pinch-off of droplet around the merging of bubbles inside the liquid film (at 15.4 ms). Similar pinch-offs happens many in number throughout the cylindrical wavy interface and generate droplet swarm in the core. The pinch-off process is well known as entrainment and its rate governs the mechanism of the dryout.

In annular flow boiling, one can visualize complicated interfacial phenomenon which is difficult to understand from the planner sectional view. For this reason, in Figure 6, a three-dimensional view of simulation has been portrayed, as representation, where the pipe is heated at 20° of superheat and liquid-vapor velocity is set at 1 and 3.4 m/s respectively (case C in Table 3). Here a 90° sector (one-fourth) of the pipe has been selected and visualized from the outer direction of the pipe (view A-A). As discussed earlier in the planar demonstration, initially due to heat transfer from the pipe wall a very thin vapor film is generated beneath the annular liquid film. But due to the gas-liquid flow, waves are generated as a result of Kelvin-Helmholtz instability and eventually, the vapor film breaks up. In Figure 6, the dark patches show the vapor nucleation sites, covered by the liquid film. The darkness of the patches on the liquid film signifies the distance of the liquid interface from the wall surface. Near the entrance, the film breaks into azimuthally symmetric vapor rims and in rest of the pipe length, it breaks into tiny vapor bubbles (at 5-10 ms). The vapor rims also further break up into asymmetric parts which due to the effect of surface tension finally contracts itself and leads to nucleation of bubbles. These vapor bubbles further flow with the liquid film and grow in size. The growth of the bubble is earlier

described in two-dimensional implementation in Figure 5. Subsequently as described earlier, when these bubbles grow beyond a certain size the liquid film above it bursts and the vapor inside it is released to the core. In Figure 6, the white spots indicate the absence of liquid film above the vapor bubbles, which demarcates the event of the bubble bursting in Figure 6. After the bubble burst, the adjacent liquid film tries to rewet the space occupied by the bubble. As a result, at a distance of 10-15 mm from the inlet, the dimension of the vapor patches seems to be reduced compared to the dimensions of the upstream vapor patches. But as the liquid film propagates along the length its thickness reduces and the rewetting capability of the film also reduces. As a result, the dry patches, generated by the bubbles bursting start growing along the length beyond 15 mm from the entry section. After 25 mm the liquid films seem to be distorted due to the enormous growth of the dry patches and some liquid lamellas are only observed at the wall surface. This phenomenon can be represented as dryout. At further downstream, these lamellas become disjoint to each other and gradually reduces in size due to continuous boiling.

One can clearly understand that the bulk behavior of dryout starts from local interfacial dynamics like bubble bursting and rewetting. The same has been demonstrated for representative two cases in the planner and in isometric interfacial profile (Figures 5 and 6, respectively). The effort has been made to understand some of these interfacial dynamics in detail. For that purpose, a case having slower interfacial evolution is targeted to get adequate temporal resolution. In Figure 7, some bubbles have been tracked for case B and they have been visualized from both direction of the liquid film (view A-A and B-B) as shown in Figure 6. In the Figure, part 7 (a) represents temporal snaps of bubble interaction with film from the outer side of the tube (i.e. A-A view) and corresponding inner side view (i.e. B-B). In the AA view, at 38 ms, two encircled bubbles can be observed in very close vicinity. While flowing with the liquid film these bubbles propagate and the distance between the bubbles reduces. As soon as these bubbles touch each other a vapor bridge is formed (38.5 ms) and gradually the bridge expands (39 ms). Finally, the bubbles get unified. As all these stages occur beneath the liquid film, these cannot be observed in B-B view, but due to the presence of the bubble, the film seems to be thicker at that zone. Due to the merging process, bubble size increases and becomes unable to accommodate itself beneath the liquid film. As a result, the liquid film above the bubble becomes thinner and finally, the bubble pierces the film above it (40 ms), which can be observed from both the views. Afterward, the perforation expands and the vapor inside the bubble gets released to the central vapor core. Once this vapor inside the bubble gets released the small dry patch left by the bubble gradually shrinks as one can see in Figure 7 (b). The phenomenon can be termed as rewetting which happens at a faster rate at the beginning (40.5-41.5 ms) and later on slows down. On the other hand, due to boiling liquid film adjacent to the dry patch loses mass, which works against the rewetting phenomenon. At 45-48.5 ms, a wave can be seen approaching the dry patch from the upstream direction. The wave helps in rewetting and shrinkage of the dry patch. As a result, at 51 ms the dry patch gets

totally rewetted, but post rewetted film thickness is much thinner as compared to the initial film thickness. It can be observed that stability of rewetting phenomena mostly depends on mutual competition between the boiling rate and interfacial waves, where the first one drags the small dry patches toward dryout and the second one tries to rewet it again. As one moves from the inlet to the exit side due to boiling film thickness reduces and the waves also become weaker. Consequently, the chance of rewetting of the dry patches reduces.

To explore the cross-sectional features in terms of interfacial evolutions, case C has been selected as representation. In Figure 8 (a) temporal evolution of annular flow has been depicted for two cross-sections at 1.09 D and 2.73 D distance from the inlet. An initially similar type of bubbles is generated azimuthally at the heated wall of both the sections. But later on (8 ms onward) lower liquid area can clearly be observed for 2.73 D compared 1.09 D. At 2.73 D the film gets disintegrated into smaller parts and these liquid patches reduce in size. On the other hand, at 1.09 D, the film remains more or less continuous other than some smaller dry patches. At 2.73 D cross-section, entrainment can also be observed (10, 50 ms), but there exists a periodicity in the passage of droplet swarm. This has created occasional dry patches at the core (entrainment absent at 35 ms), whenever a cross-section is in-between regions of two traveling droplet swarms.

To have a more comprehensive view over the cross-sections, in Figure 8 (b) liquid phase has been plotted at a particular time (37.5 ms) but for different cross-sectional planes. The non-dimensionalized distance of the cross-sectional planes from the inlet plane has been inscribed inside the Figures in terms of pipe diameter.

As one can see, starting from uniform thickness annular entry at 0.45D, a huge number of tiny bubbles are formed near the wall. With further advancement in the axial direction (0.73 D) the number of bubbles in the cross-section reduces but bubble size increases due to growth and mutual merging. In the subsequent higher sectional views (1.09 D – 1.45 D), due to the bubble bursting the film becomes azimuthally discontinuous. Gradually, these discontinuities grow in number and length, as a result, the liquid film shrinks into thinner patches (2.09 D). At further downstream, liquid entrainment has been observed at the core of the cross-sectional views. These entrained liquid drops are randomly distributed over the whole space. Initially, this droplet population seems to be increasing with axial distance (2.73 D – 3.18 D) but once the liquid patches on the wall reduce droplet population also reduces gradually (4.09 D – 4.54 D) due to evaporation of mist flow.

3.2. Quantification of bubble size:

From the results of interfacial behavior, efforts have been made to evaluate specific bubble dynamics in terms of growth rate and merging tendency. The spatial distribution of size for vapor bubbles across the length of the tube is as shown in Figure 9 (a). To quantify the bubble size in terms

of contact bubble radius, the volume of the vapor bubble is converted to be equivalent to the radius of a hemisphere. The Figure shows continuously increasing bubble size attached to the wall, as one moves up axially. Along with growth bubble are translating in the axial direction which results in a progressive increase in contact radius along the tube wall. Only a small swelling in the thin vapor film can be observed at point 1. Due to change of phase, the vapor is fed to the nucleation causing growth and liquid inertia shifts the nucleation at point 2. As a result, at location 2, comparatively larger bubble size than point 1 is observed. This procedure continues until two axially neighboring bubbles get closer. The continuous increase in the trend of bubble radius, in Figure 9 (a), along with axial location demonstrates the same. At point 9 along the axial direction, one can notice a sudden jump in contact radius of the bubble which may be resultant of merging between neighbors. This can be clearly understood from the temporal growth history of a bubble which has been plotted in Figure 9 (b). After point 10, the bursting of the bubble occurs from which point measurement of the bubble radius is not feasible. As a result, the axial growth distribution of the bubble has been only shown till point 10. Dryout sets in after this axial location.

The temporal history of bubble growth has been expressed in terms of contact length along the axial direction of solid at different phases of the bubble lifecycle. As the bubble is starting to grow from the asymptotic film, at the beginning contact length seems to be reduced from an infinitely large value. Soon due to the growth of the truncated spherical sized bubble, one can see almost linear increase history of contact length. The pattern of growth in contact length continues until the departure of the bubble or merging with the neighbor happens. In that case, a sharp increase in contact length has been reported in Figure 9 (b). At a few time instances, the shape and size of bubbles are reported in Figure 9 (b).

To observe the fluid dynamics around two bubbles indulging in the merging process, efforts have been made to identify and track advancing and receding fronts as shown in Figure 10. As during nucleation (9.1 ms) both the bubbles start from a film, these are supposed to have almost no liquid bridge between them at a very high radius of curvature. With growth, these bubbles first go away from each other signifying a reduction in radius of curvature and an increase in the mutual gap. Once these bubbles attain hemispherical shape due to a continuous supply of vapor, the radius of curvature starts to increase and bubbles come closer to each other. This will reduce the gap between bubbles by driving away the film. In this phase, advancing front of succeeding bubble and receding front of the preceding bubble will come closer to each other. At the time instance of merging (14 ms), these two ends of bubbles coincide to initiate the unification process. Due to the flow of liquid both the bubbles are seen to move up even during the merging process which causes an increase in axial location of advancing and receding fronts of succeeding and preceding bubbles. Figure 10 describes the overall merging process along with an account of the gap between the bubbles.

3.3. Dryout length prediction with parametric variation:

To observe the effect of parametric variation on liquid film evolution across the pipe length in Figure 11 comparison of the same has been studied for the same time instant (62.5 ms) from A-A direction. In Figure 11 (a) comparison of three degrees of superheats has (10, 20 & 50°C) been portrayed. One can clearly observe from the Figure that dryout length is continuously decreasing from ~3D (35 mm for 10°C) to ~1.5D (15 mm for 50°C) with an increase in wall degree of superheat. At a higher degree of superheat, due to a higher rate of boiling, increase in bubble diameter has also been observed beneath the liquid film. Close look on the post dryout region also shows that the size of the lamellas generated from the liquid film decreases at a higher degree of superheat. Effect of flow conditions on interfacial evolution has been also studied and some representative liquid distribution along axial lengths are shown in Figure 11 (b). Comparison of case C and H shows that at the higher liquid velocity the film dryout is delayed. Moreover, at higher liquid flow bubble bursting and rewetting zone is also shifted downstream. Variation of vapor flow rate can also be observed by comparing interfacial contours for the cases A, C, E, and F. Among cases A, C and E significant change in dryout length has not been observed, but with an increase in flow rate, nature of post dryout lamellas has changed to a thinner one. But for case F due to very high gas velocity liquid film got disrupted and dryout occurred well before compared to A, C, and D. This dryout is not due to boiling, but entrainment due to high gas velocity leads the liquid film toward dryout. Here, high gas velocity tears liquid film into smaller parts, as a result, elongated lamellas are not found in the post dryout region.

3.4. Quantification of vapor and liquid distributions in the domain:

The effect of bubble nucleation and its bursting at the annular film surface can be clearly understood from the percentage of vapor present in the annular liquid domain, given as initial condition. Nucleation and its growth will generate vapor inside annular film from the side of the wall due to heat transfer. On the other hand, the formation of a wave due to the relative velocity of liquid and vapor will allow gaseous vapor to penetrate from the core side of the annular film. Bursting of a growing bubble in the inner film adds on the situation and drastically increases vapor presence through the phase of dryout. These three processes are a major reason for an increment of a percent in vapor present in the annular film. On the other hand, hot tube wall rewetting by liquid lowers the presence of vapor in the liquid region. Initially, due to heat transfer, the conducive situation for vapor formation increases the percentage presence as time progresses. Once the rewetting starts from local dryout sites presence of local annular film becomes more or less Table. Similar pattern has been shown in Figure 12 (a), where at the beginning increasing trend of vapor presence has been observed for different degrees of superheat and then the presence of vapor in liquid film region gets Table. Comparison between three different degrees of superheats (10, 20, 50 °C; Case B, C, D) clearly depicts faster vapor intrusion in the liquid region with an increase in superheat. Bubbles are nucleated and burst at a faster rate at a high degree of

superheat and reached to a higher percentage of steady-state vapor presence in the liquid region, given at the beginning of the simulation. At a steady-state, the percentage of vapor present in the liquid region increases with an increase in superheat.

Similar efforts to study the present presence of vapor volume in the annular region have been reported for varying liquid and vapor inflows (Figure 12 (b)) with an increase of vapor velocity (case C to case F) faster decrease in liquid occupancy is observed in the annular region. This symbolizes more frequent dryout spots at higher vapor velocities. It can be also noted that even at steady state percent of vapor volume in terms of initial annular liquid volume is higher for higher values off vapor velocities. On the other hand, when liquid velocity increased there is the lesser provision of disturbance wave and formation of vapor in the annular liquid region will be mainly governed by the nucleating bubble. Due to the reduction of amplitude in a wave from core side lesser vapor penetration will be there in the annular liquid when liquid velocity is increased (case C to case H). As a result, case H will stabilize at a further lower percent of vapor presence than case C. More rewetting can be observed at higher liquid velocities along with lesser bubble bursting stages.

Inventory of liquid and vapor has been also monitored at the different cross-sectional planes of the simulation, which may have randomly changing values due to transient interfacial dynamics. Figure 13 (a)-(b) depicts the presence of liquid in a few cross-sectional planes in terms of phase fraction for case C, as representative. At the inlet, due to the boundary condition, the liquid phase fraction remained constant. Afterward, lines for different cross-section starts reducing due to boiling. In parallel, some fluctuating components can also be observed in the plots at a different plane, which is mainly due to wave and bubble passage through the cross-sections. At the very initial stage passage of these waves can be clearly seen from the zoomed comparison of volume fraction history at different volume fraction planes. A peak in wave signifies the passage of disturbance wave in a cross-section and increase of the peak magnitude of liquid phase fraction shows continuous development of amplitude of disturbance wave. The disturbance wave reaches a later time in higher axial locations than 0.91D. In the later stages, these disturbance waves go away and interfacial phenomena mainly become dominated by vapor dynamics generated from the hot wall. Continuous breaking and making of these interfaces as described above will give rise lots of fluctuations in the account of liquid presence. The same can be seen in Figure 13 (a). These disturbances in liquid phase fraction will fluctuate around a steady value due to a similar rate of making of the interface during nucleation and breaking of the same during bursting. For case C, shown as representation, abrupt fluctuations due to disturbance wave goes away from the computational domain and volume fraction attains pseudo-steady value around 40 ms. At this steady-state condition, a distinct range of phase fraction value for each cross-section can be identified from Figure 13 (b). In the signals, shown in Figure 13 (b), it can be clearly identified that with an increase in distance from the inlet section range of liquid phase fraction value shifts toward a lower value.

Efforts have been made to understand the details of these fluctuations by mathematical analysis of the same. To begin with, in Figure 14 (a), the average value of the temporal variation of the liquid phase fraction has been reported against the axial distance from the inlet. Account of average liquid volume fraction variation across axial distance is reported for three different degrees of wall superheat (Case B, C, and D). The average value of liquid fraction decreases continuously as the flow moves up, which is evident from the effect of heat transfer and subsequent phase change. In all three cases, one can observe instantaneous dryout at some azimuthal locations followed by rewetting by liquid packets. A careful comparison between average values at different degrees of superheat reveals that dryout occurs more frequently and azimuthally at a greater number of places while higher (50°C) superheat is applied, causing temporal average of liquid phase fraction value to reach very near to zero. It is also observed that at a higher degree of superheat the liquid fraction reduces faster along the length. A close look at the trend of these plots reveals a lower slope region near to the entrance, after that the slope of increases and post dryout slope reduces again. One can refer to Figure 6, where dryout happens near 30 mm distance from the entrance and in Figure 14 (a) also the slope of the 20°C (Case C) superheat line reduces at almost same axial position (~ 30 mm). To understand the reason behind fluctuating values of liquid phase fraction, the standard deviation of the same has also been plotted in Figure 14 (a). Due to uniform and constant inlet velocity boundary condition near the entrance standard deviation is very small. Afterward, as the flow propagate away from the entrance, due to wave and vapor bubble generation, the standard deviation of the liquid fraction rises up to a certain value. But soon dryout triggers in and liquid quantity left in the domain becomes very small. As a result, fluctuation in liquid fraction reduces and standard deviation becomes lower. From Figure one can observe that standard deviation for 20°C and 50°C superheat does not show much difference in value but for 10°C superheat one sharp peak is obtained. This peak is due to the formation of bigger lumps of liquid from the liquid film under the presence of a lower evaporation rate. But in case of the higher degree of superheat liquid film dries up faster and only smaller lamellas can form instead of bigger lumps. As a result, such a peak of standard deviation is not observed in higher degrees of superheat (Case C & D).

A similar effort has been made to observe the effect of vapor flow on average liquid phase fraction. In Figure 14 (b), the mean and standard deviation of liquid phase fraction for three different vapor velocities (2.5 m/s, 3.4 m/s and 4.5 m/s) have been shown against axial distance. Though the difference in this case is not that distinct as compared to the variation of the degree of wall superheat, still at higher vapor flow rate faster drop in cross-sectional average liquid phase fraction can be clearly noticed. At higher vapor flow rate liquid film will also be accelerated, which finally helps in enhancing convective heat transfer and subsequently results in a higher rate of boiling. On the other hand, the standard deviation curves for 3.4 and 4.5 m/s vapor velocities nearly show a similar pattern but as the vapor velocity is reduced to 2.5 m/s, the vapor is unable to drag the liquid film effectively. As a result, the film transforms into larger liquid lumps leading to a higher value to standard deviation.

To have a comprehensive view of the variation in liquid phase fraction, attractor, a plot of ($\beta_{L, x,t + \Delta t}, \beta_{L, x,t}$), has been carefully studied, where liquid phase fraction has been mapped to itself after non-dimensionalisation as $\beta_{L, x,t} = \alpha_{L, x,t} / \alpha_{L, x=0,t}$. In Figure 15 (a) attractor plot for different cross-sections of 20°C superheat has been demonstrated. Near the inlet (10 mm) all the mapped data points of the attractor plot are concentrated over small region. Afterward, as flow moves at 20 mm from the inlet, data points spread towards the origin. Thereafter, at 30 mm the range of liquid phase fraction sharply drops and a similar trend has been followed for further axial locations from inlet keeping nature of scattering intact. At 50 mm, attractor plot data points again accumulate over a smaller area near the origin, because due to complete dryout fluctuations also have died down significantly. Comparison of attractors at different planes shows the tendency of liquid phase fraction towards dryout and fluctuations are reported through scatter in the intermediate axial lengths, away from inlet and dryout locations.

In Figure 15 (b), a mutual comparison of the attractor plots for different degrees of superheat has been presented. It can be observed that for 10°C many data points cross the inlet liquid fraction value marked by the red dotted line. Even some data points for axial distance 30 mm are crossing the inlet phase fraction and some others are also extended till 0.5 value, which shows the extent of dispersion of the data points. This also shows randomness in the interfacial evolution through breaking and making, in the whole span of bubble life-cycle. On the contrary, in case of 50°C superheat all the data points of the attractor plot are much below the red dotted line (phase fraction at inlet) and they are accumulated within smaller areas showing lesser randomness and quick reach towards dryout.

3.5. Heat transfer coefficient plots:

An effort has been also made to understand the thermal analysis of interfacial making and breaking process. To characterize the same, the average heat transfer coefficient (HTC) at different axial planes have been evaluated from simulations. An axial variation of the same has been plotted in Figure 16 (a) & (b). For mutual comparison of heat transfer characteristics between different applied degrees of superheat at the wall, in Figure 15 (a), plots are shown for 10, 20 & 50 °C (Case B, C & D). Careful analysis of each curve shows an initial drop of heat transfer coefficient for a very prompt period. This has resulted from the formation of thin vapor cover throughout the domain at a lower axial length. As flow progresses in a higher axial domain, vapor film becomes thicker due to buoyancy and instability triggers in nucleation. In this region of axial location, due to the release of vapor and replenishment of liquid from the film, the heat transfer coefficient has been seen to be increased. Such nucleation and growth process continues up to a certain length before bubble bursts at annular interfacial surface. This results in a small drop in the heat transfer coefficient for all the applied degrees of superheat in the wall. As a next consequence, rewetting happens which increases the heat transfer coefficient from dryout in a very prompt zone. But this rewetting will diminish its effect due to more and more dryout spots

created in different azimuthal locations. Hence, in heat transfer pattern a continuous decrease is noticed signifying more and more dryout spots as flow moves up axially.

A careful comparison between different curves in Figure 16 (a), for variable degrees of superheats, establishes a lesser span of the axial zone for nucleation for a higher degree of superheat. The heat transfer coefficient throughout the tube reduces drastically for an increase in the applied degree of superheat due to an increased rate of change of phase. It can be also noticed that at higher degree of superheat heat transfer coefficient is nearing towards a very small value, owing to arriving at faster dryout. similar trend is seen for average heat transfer coefficient for different liquid and vapor velocities.

At higher liquid velocity nucleation and bursting of bubbles at higher axial heights causing delay in reaching the highest heat flux. As the superheat is the same in both liquid velocities, the maximum average heat transfer coefficient has been also noticed as same. But in the dryout zone higher liquid velocity shows better heat transfer coefficient due to better transport of heat. On the other hand, at higher vapor velocity (case F) film becomes thinner causing bursting and dryout faster than the same in low liquid velocity (case C). Figure 16 (b) also shows that the average heat transfer coefficient may fall to a very low value in case of high vapor velocity.

4. Conclusion:

In the present study, annular flow boiling has been studied numerically for different degrees of superheats and flow conditions. Some of the significant inferences, which can be inferred from this study are tabulated below.

- i. In the annular flow boiling small bubbles are generated beneath the liquid film and they grow due to boiling and merge among themselves.
- ii. When the bubbles grow comparable to the film thickness, they burst and small dry patches are generated. Waves on liquid film try to rewet the dry patches but boiling tries to expand them. The relative strength of them finally decides the fate of the dry patch, whether it will be rewetted or be expanded to dryout condition.
- iii. Rewetting enhances heat transfer but its length reduces with a higher degree of superheat, leading the flow toward early dryout.
- iv. Entrainment of liquid drops and lamellas observed from the waves of the liquid film. Maximum entrainment of the liquid has been observed near the dryout region. The post dryout droplet population gradually reduces in the axial direction.
- v. Stronger waves and higher temporal fluctuation of phase fraction has been observed for a lower degree of superheat. On the other hand, at a higher degree of superheat liquid phase fraction shows faster decrement with less fluctuation.

- vi. The heat transfer coefficient shows axial variation before dropping down to a very low value as observed in dryout. Higher degrees of superheat, lesser liquid flow rate and higher vapor flow rate may lead towards the very small value of heat transfer coefficient signifying dryout.

Declaration of competing interest

The authors declare that they have no known competing financial interests or personal relationships that could have appeared to influence the work reported in this paper.

Acknowledgment:

The present research work is funded by project no. 36(1)/14/55/2016-BRNS/36/28 sponsored by Board of Research in Nuclear Science, Department of Atomic Energy, Mumbai, India

References:

- Adamsson, C. and Le Corre, J.M., 2011. Modeling and validation of a mechanistic tool (MEFISTO) for the prediction of critical power in BWR fuel assemblies. *Nuclear Engineering and Design*, 241(8), pp.2843-2858.
- Albadawi, A., Donoghue, D.B., Robinson, A.J., Murray, D.B. and Delauré, Y.M.C., 2013. Influence of surface tension implementation in volume of fluid and coupled volume of fluid with level set methods for bubble growth and detachment. *International Journal of Multiphase Flow*, 53, pp.11-28.
- Andreani, M. and Yadigaroglu, G., 1994. Prediction methods for dispersed flow film boiling. *International journal of multiphase flow*, 20, pp.1-51.
- Anglart, H., Ji, W. and Gu, C.Y., 1997. Numerical simulation of multidimensional two-phase boiling flow in rod bundles. In Eighth international topical meeting on nuclear reactor thermal-hydraulics.
- Barbosa Jr, J.R., Hewitt, G.F. and Richardson, S.M., 2003. High-speed visualisation of nucleate boiling in vertical annular flow. *International journal of heat and mass transfer*, 46(26), pp.5153-5160.
- Becker, K.M., Ling, C.H., Hedberg, S. and Strand, G., 1983. *An experimental investigation of post dryout heat transfer* (No. KTH-NEL--33 (V. 1, 2)). Royal Inst. of Tech.
- Brackbill, J.U., Kothe, D.B. and Zemach, C., 1992. A continuum method for modeling surface tension. *Journal of computational physics*, 100(2), pp.335-354.
- Chi-Liang, Y. and Mesler, R.B., 1977. A study of nucleate boiling near the peak heat flux through measurement of transient surface temperature. *International Journal of Heat and Mass Transfer*, 20(8), pp.827-840.
- Collier, J.G. and Thome, J.R., 1994. *Convective boiling and condensation*. Clarendon Press.

- Del Valle, V.H. and Kenning, D.B.R., 1985. Subcooled flow boiling at high heat flux. *International Journal of Heat and Mass Transfer*, 28(10), pp.1907-1920.
- El-Genk, M.S. and Saber, H.H., 2001. Minimum thickness of a flowing down liquid film on a vertical surface. *International Journal of Heat and Mass Transfer*, 44(15), pp.2809-2825.
- Emonot, P., Souyri, A., Gandrille, J.L. and Barré, F., 2011. CATHARE-3: A new system code for thermal-hydraulics in the context of the NEPTUNE project. *Nuclear Engineering and Design*, 241(11), pp.4476-4481.
- Glück, M., 2007. Sub-channel analysis with F-COBRA-TF-Code validation and approaches to CHF prediction. *Nuclear Engineering and Design*, 237(6), pp.655-667.
- Hoyer, N., 1998. Calculation of dryout and post-dryout heat transfer for tube geometry. *International journal of multiphase flow*, 24(2), pp.319-334.
- Ishii, M. and Denten, J.P., 1990. Two-phase flow characteristic of inverted bubbly, slug and annular flow in post-critical heat flux region. *Nuclear Engineering and Design*, 121(3), pp.349-366.
- Jayanti, S. and Hewitt, G.F., 1997. Hydrodynamics and heat transfer in wavy annular gas-liquid flow: a computational fluid dynamics study. *International Journal of Heat and Mass Transfer*, 40(10), pp.2445-2460.
- Klostermann, J., Schaake, K. and Schwarze, R., 2013. Numerical simulation of a single rising bubble by VOF with surface compression. *International Journal for Numerical Methods in Fluids*, 71(8), pp.960-982.
- Kumar, P., Das, A.K. and Mitra, S.K., 2016. Physical understanding of gas-liquid annular flow and its transition to dispersed droplets. *Physics of Fluids*, 28(7), p.072101.
- Lafaurie, B., Nardone, C., Scardovelli, R., Zaleski, S. and Zanetti, G., 1994. Modelling merging and fragmentation in multiphase flows with SURFER. *Journal of Computational Physics*, 113(1), pp.134-147.
- Li, D. and Dhir, V.K., 2007. Numerical study of single bubble dynamics during flow boiling. *Journal of Heat transfer*, 129(7), pp.864-876.
- Li, H. and Anglart, H., 2016A. Prediction of dryout and post-dryout heat transfer using a two-phase CFD model. *International Journal of Heat and Mass Transfer*, 99, pp.839-850.
- Li, H. and Anglart, H., 2016B. Modeling of annular two-phase flow using a unified CFD approach. *Nuclear Engineering and Design*, 303, pp.17-24.

- Marek, R. and Straub, J., 2001. Analysis of the evaporation coefficient and the condensation coefficient of water. *International Journal of Heat and Mass Transfer*, 44(1), pp.39-53.
- Mukherjee, A. and Dhir, V.K., 2004. Study of lateral merger of vapor bubbles during nucleate pool boiling. *J. Heat Transfer*, 126(6), pp.1023-1039.
- Pandey, V., Biswas, G., Dalal, A., and Welch, S. W. J., 2018. "Bubble lifecycle during heterogeneous nucleate boiling". *Journal of Heat Transfer (ASME)*, 140(12), p. 121503.
- Plessset, M.S. and Zwick, S.A., 1954. The growth of vapor bubbles in superheated liquids. *Journal of applied physics*, 25(4), pp.493-500.
- Samkhaniani, N. and Ansari, M.R., 2017. Numerical simulation of superheated vapor bubble rising in stagnant liquid. *Heat and Mass Transfer*, 53(9), pp.2885-2899.
- Sato, Y. and Niceno, B., 2015. A depleTable micro-layer model for nucleate pool boiling. *Journal of Computational physics*, 300, pp.20-52.
- Sugawara, S. and Miyamoto, Y., 1990. FIDAS: Detailed subchannel analysis code based on the three-fluid and three-field model. *Nuclear Engineering and Design*, 120(2-3), pp.147-161.
- Sugawara, S., Sakai, T., Watanabe, K. and Rummens, H.E.C., 1991. Subchannel analysis by the FIDAS code based on the three-fluid model. *Nuclear engineering and design*, 132(2), pp.253-264.
- Tanasawa, I., 1991. Advances in condensation heat transfer. In *Advances in heat transfer* (Vol. 21, pp. 55-139). Elsevier.
- Tong, L.S., 2018. *Boiling heat transfer and two-phase flow*. Routledge.
- Utaka, Y., Kashiwabara, Y. and Ozaki, M., 2013. Microlayer structure in nucleate boiling of water and ethanol at atmospheric pressure. *International Journal of Heat and Mass Transfer*, 57(1), pp.222-230.
- Valette, M., Pouvreau, J., Bestion, D. and Emonot, P., 2011. Revisiting large break LOCA with the CATHARE-3 three-field model. *Nuclear Engineering and Design*, 241(11), pp.4487-4496.
- Van Leer, B., 1974. Towards the ultimate conservative difference scheme. II. Monotonicity and conservation combined in a second-order scheme. *Journal of computational physics*, 14(4), pp.361-370.
- Weller, H.G., 2008. A new approach to VOF-based interface capturing methods for incompressible and compressible flow. OpenCFD Ltd., Report TR/HGW, 4.
- Yang, J., Narayanan, C. and Lakehal, D., 2017. Large Eddy & Interface Simulation (LEIS) of disturbance waves and heat transfer in annular flows. *Nuclear Engineering and Design*, 321, pp.190-198.

Journal Pre-proofs

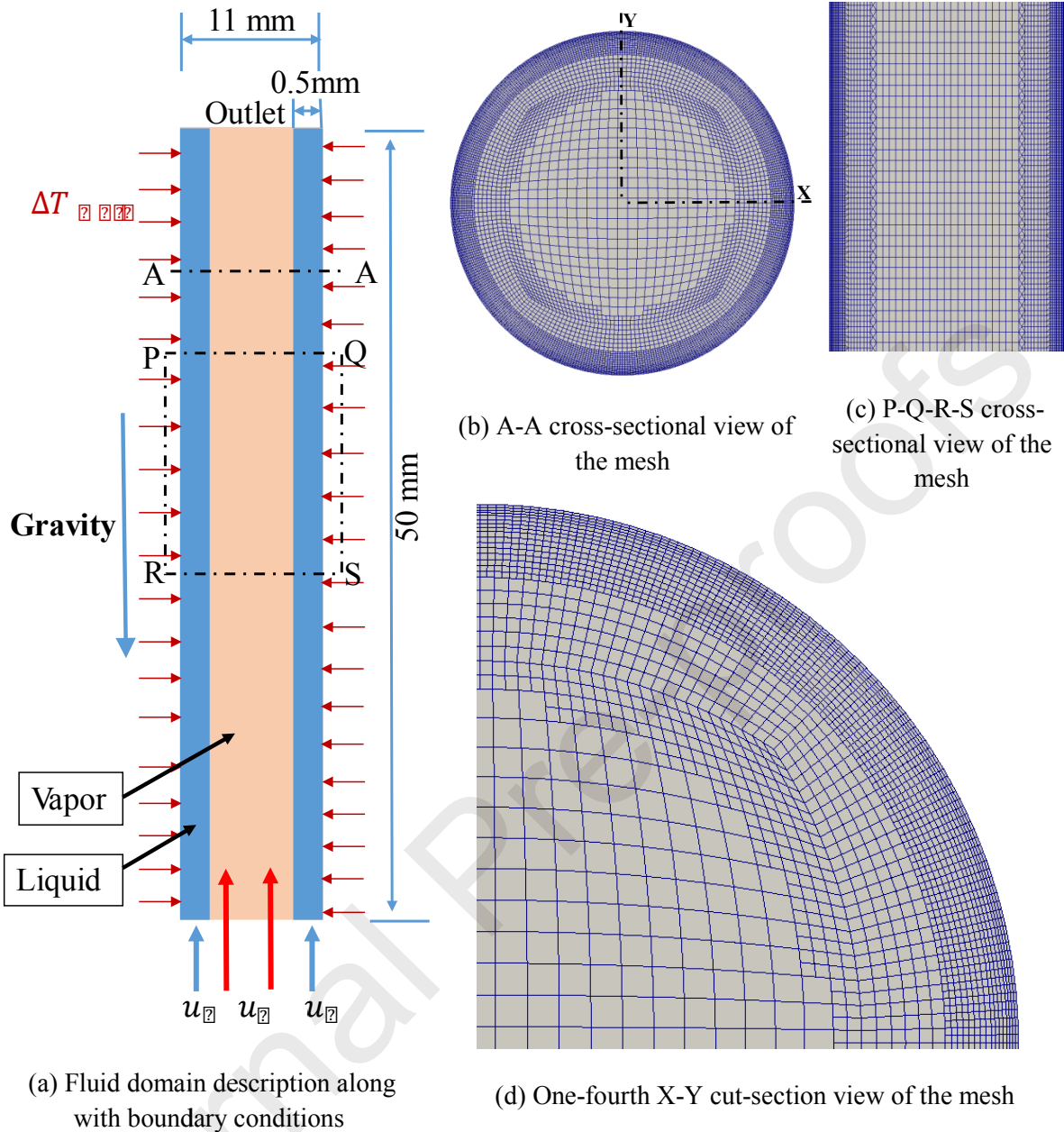


Figure 1: Domain description and mesh configuration

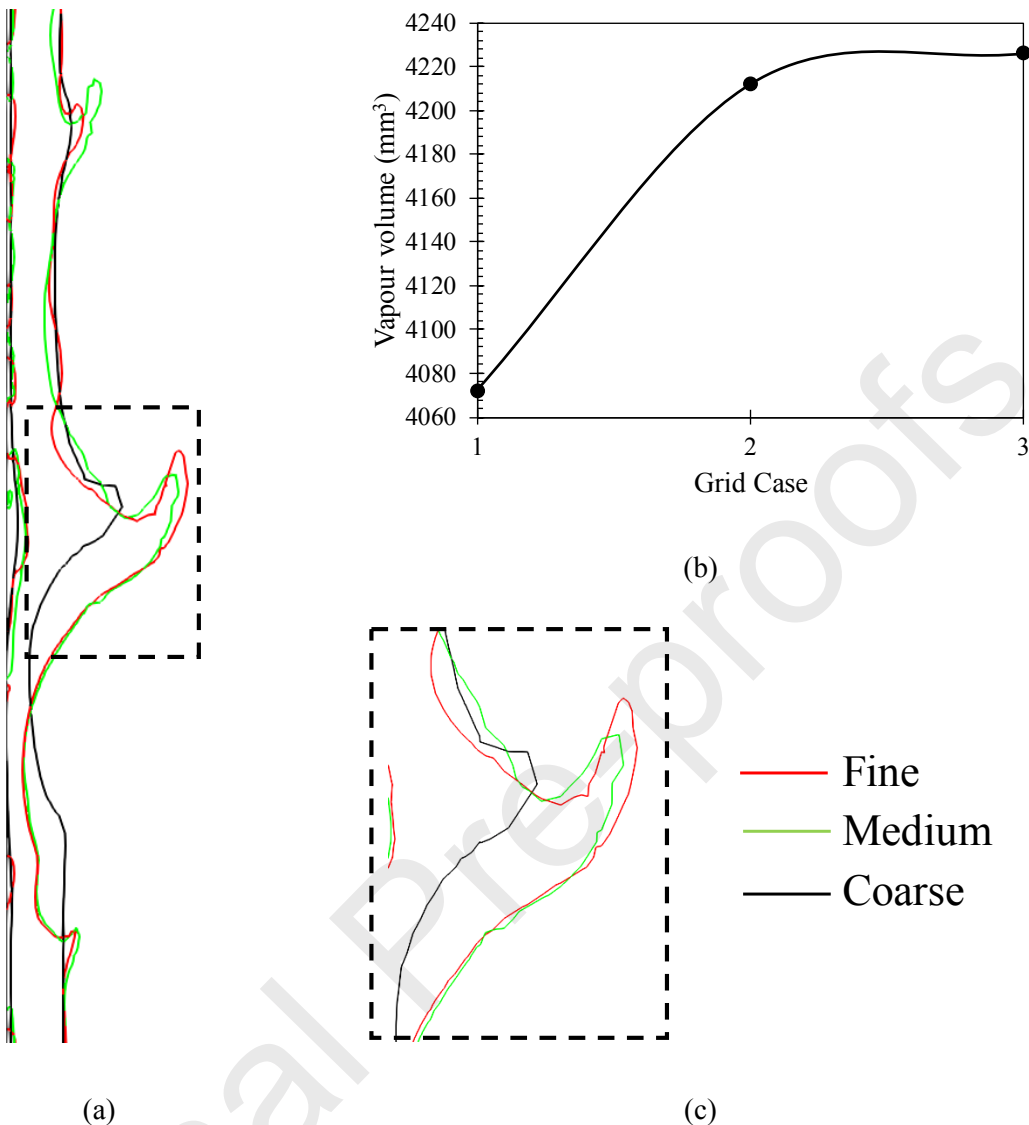


Figure 2: Grid independent study (a) interfacial dynamics for coarse, medium and fine (b) quantification of grid independent study (c) zoomed view of the zone indicated with dashed line

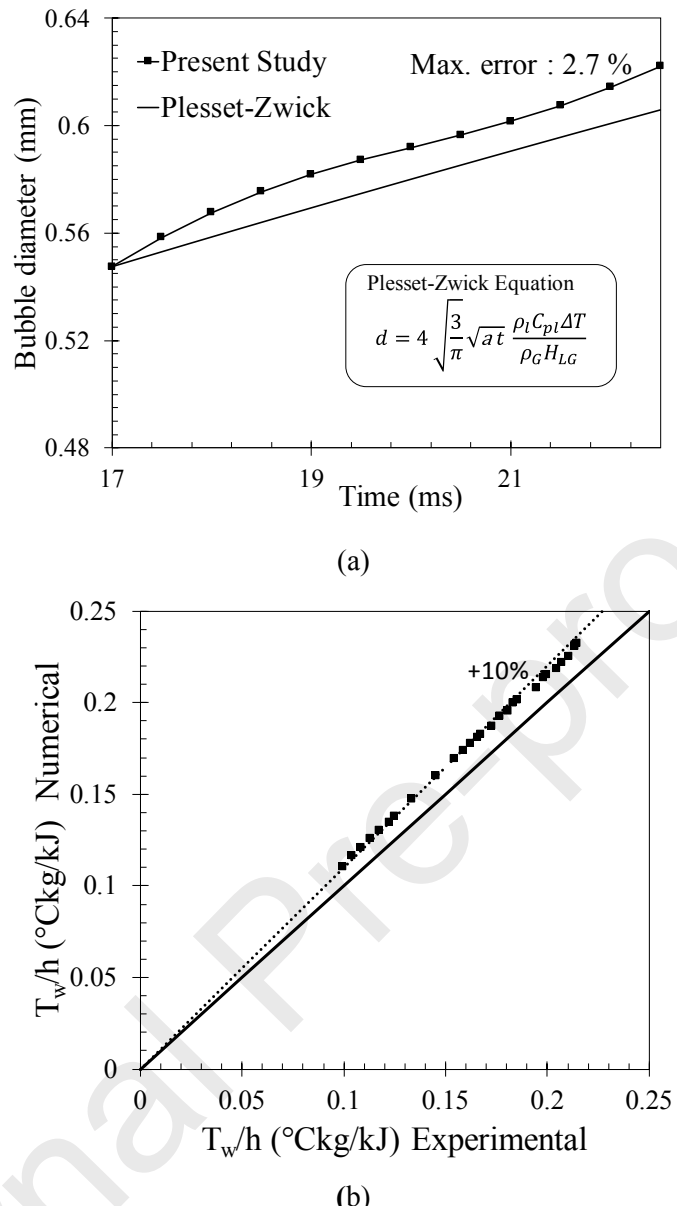


Figure 3: Validation plots (a) comparison of bubble diameter (d) calculated with Plessset-Zwick equation and the present study for a single bubble (b) comparison of numerically calculated ratio of wall temperature and enthalpy with experimental values for annular flow boiling

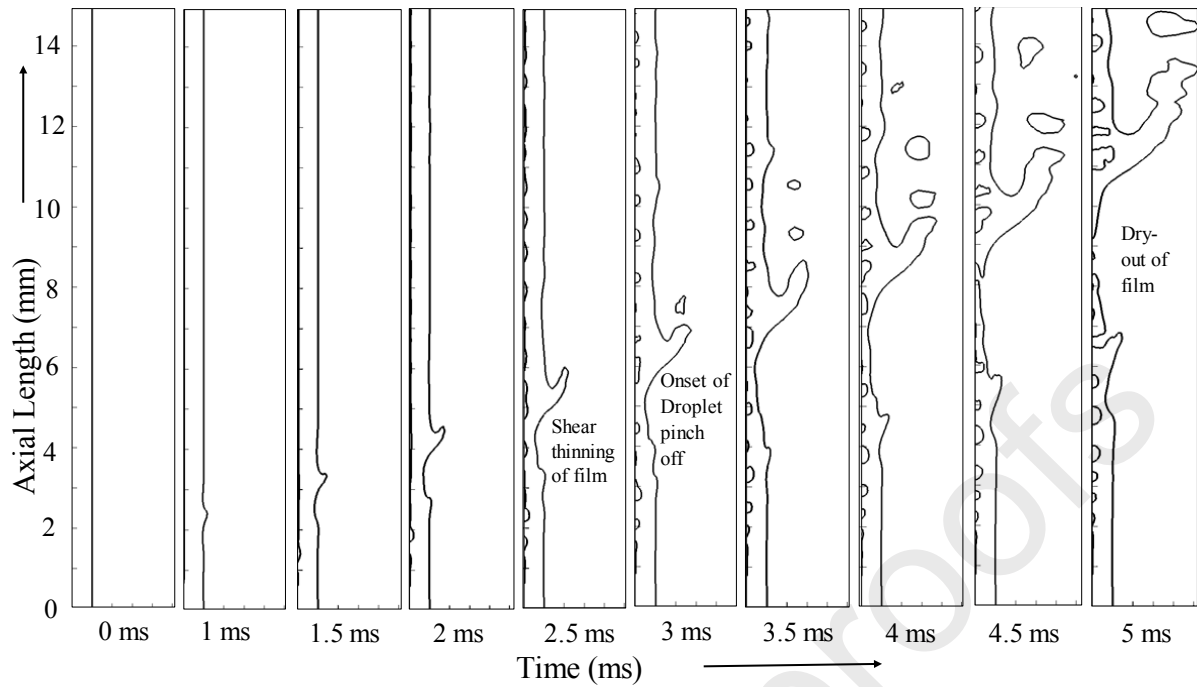


Figure 4: Liquid vapor interfacial dynamics for water inside a tube; VOF contour is shown in one half of the axial plane. Simultaneous initiation of vapor bubble and liquid drop can be observed as an aftermath of inertial disturbance wave and phase change. Mechanism of dryout is also highlighted.

(for case G in table 3)

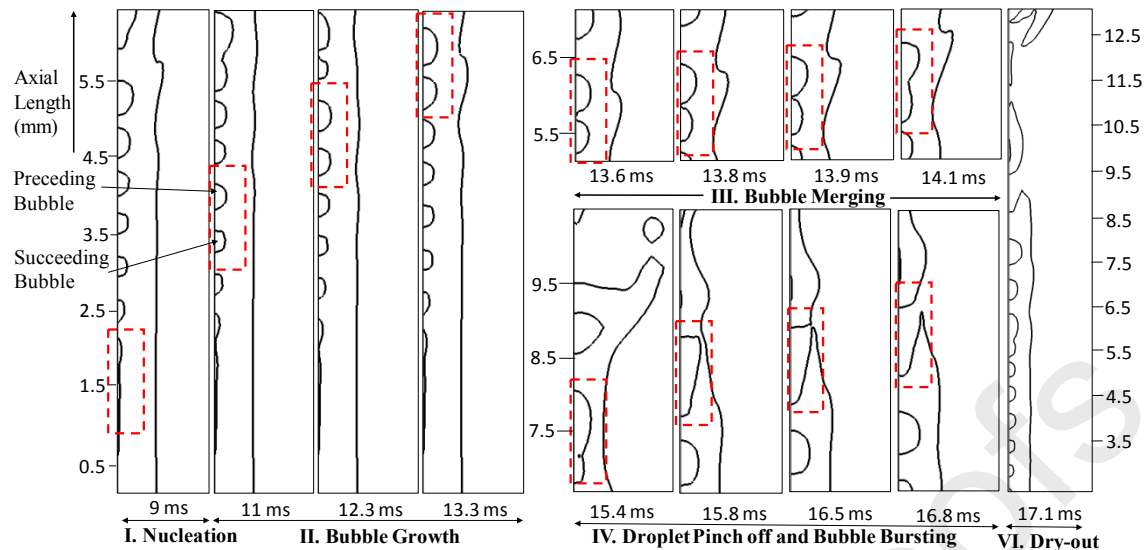


Figure 5: On-route to dry-out through stages of bubble evolution (case G in table 3)

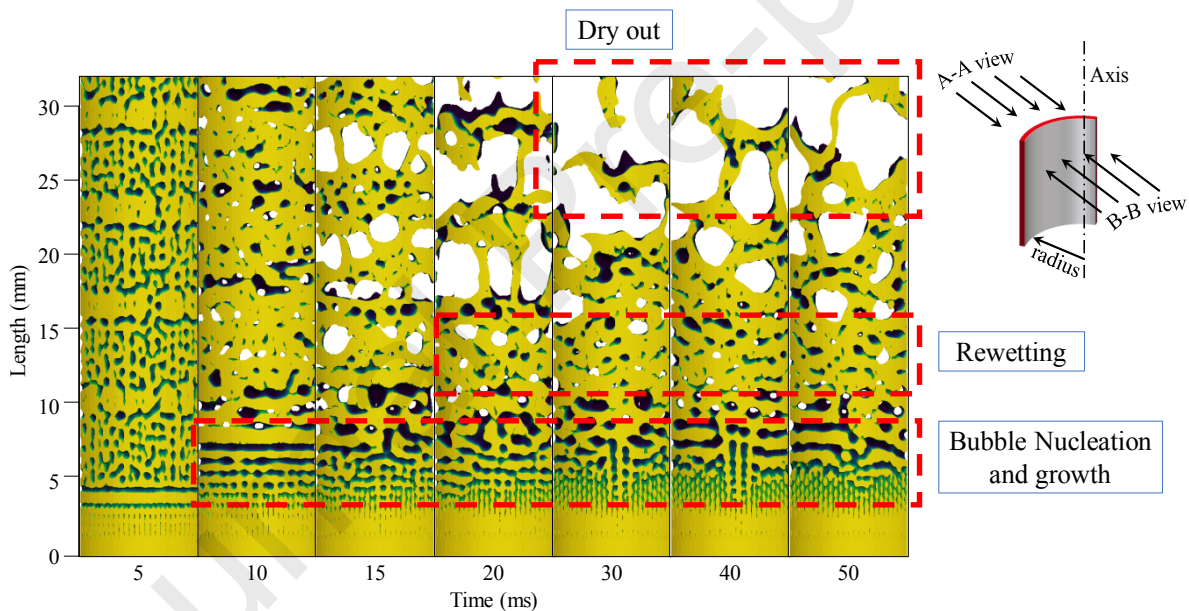


Figure 6: Three-dimensional view (from AA direction) of the temporal evolution of liquid film across the pipe length

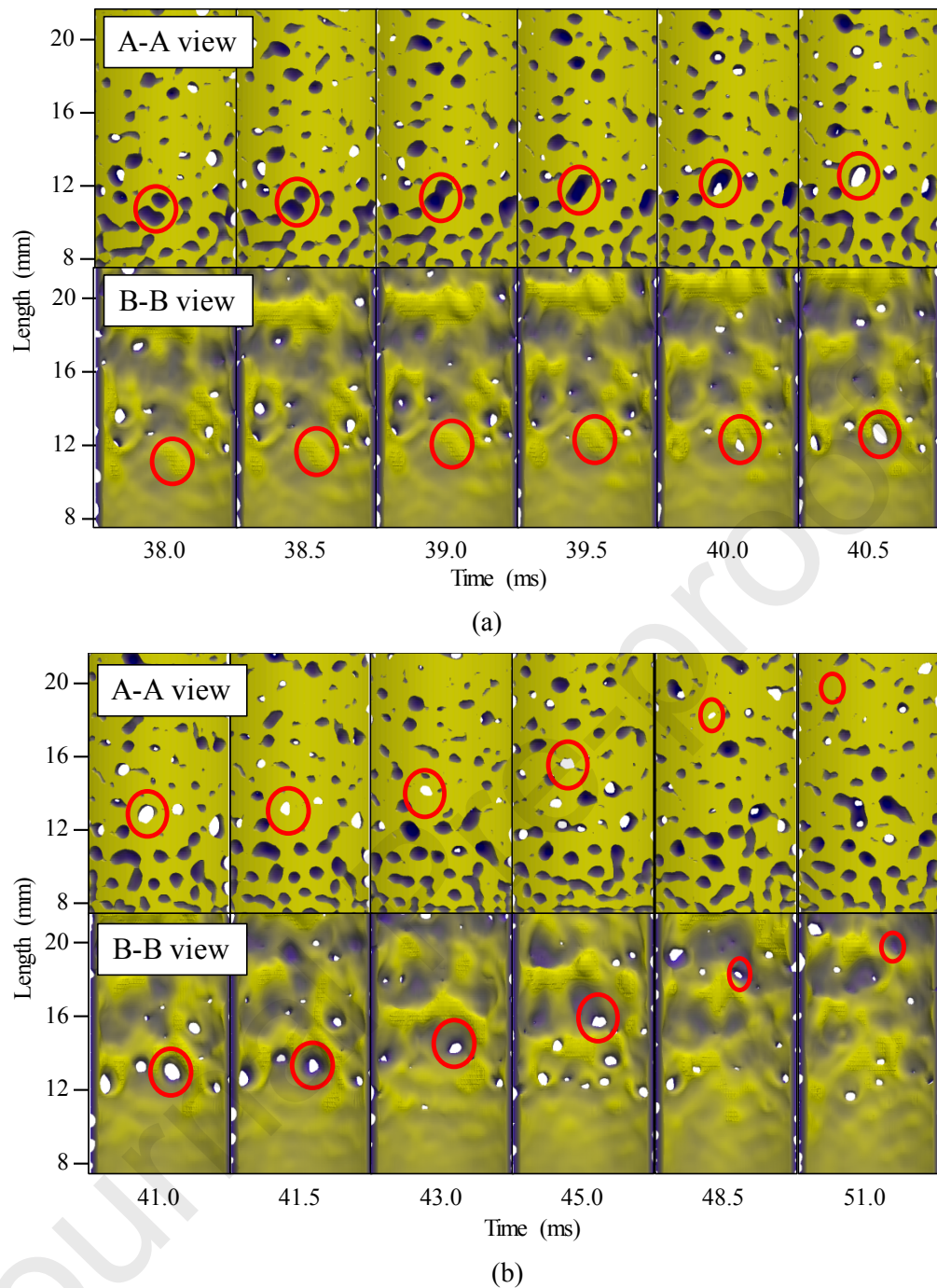


Figure 7: Interfacial evolution during two important features responsible for dry out (a) bubble merging and bursting (b) rewetting

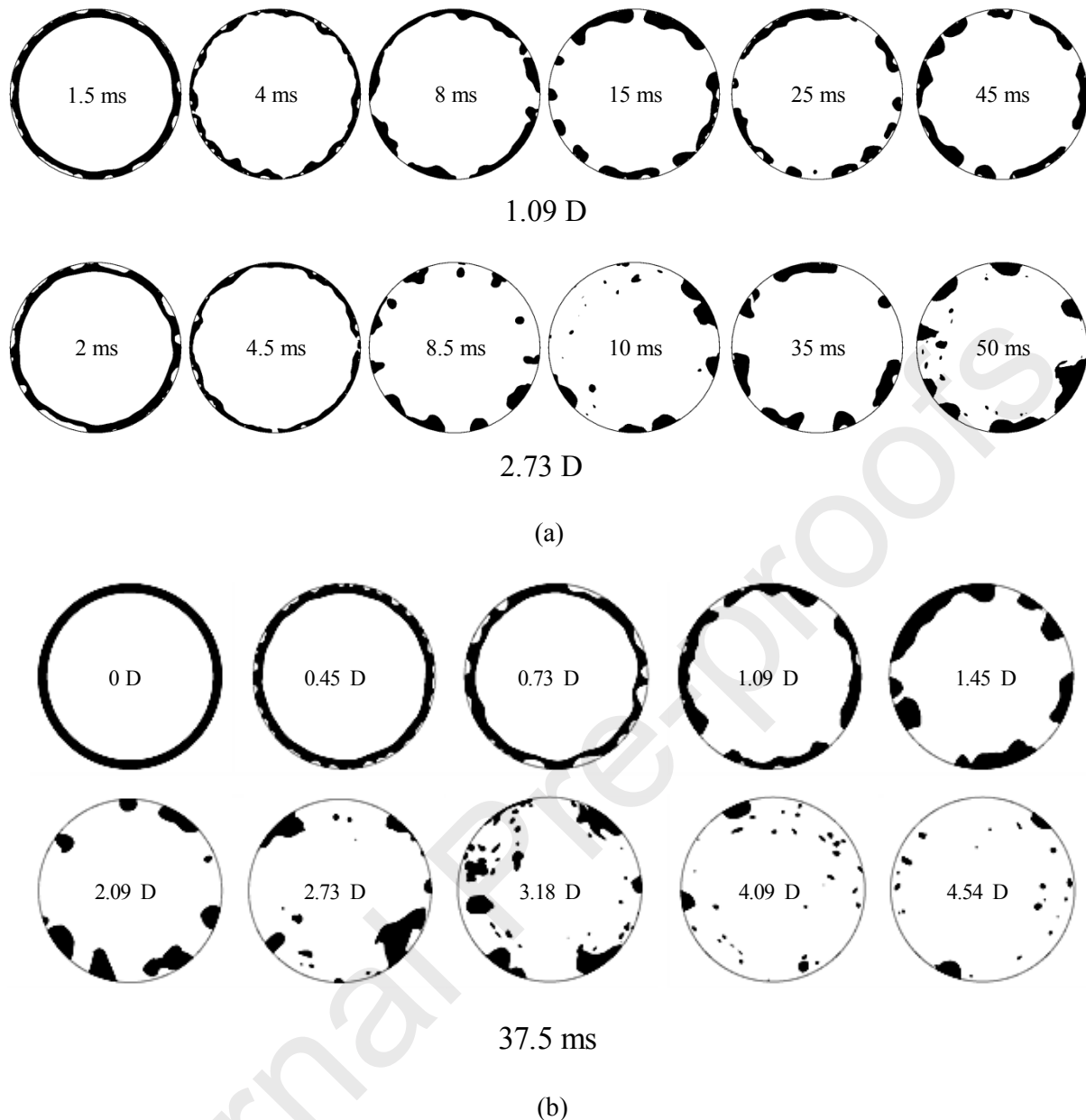


Figure 8: Cross-sectional view of annular to droplet flow (a) at different time instant (b) at different axial distance; wall flooding, dry out and droplet population can be clearly observed.

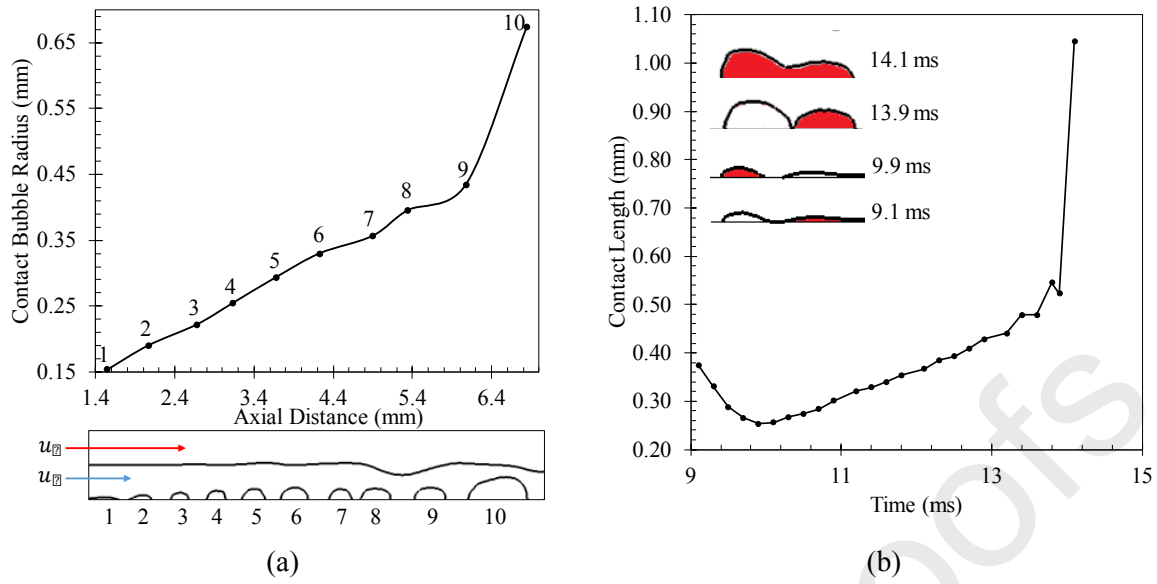


Figure 9: Characteristics of bubble growth (a) gradual increase of contact radius along with axial length (b) temporal history of growth at a site

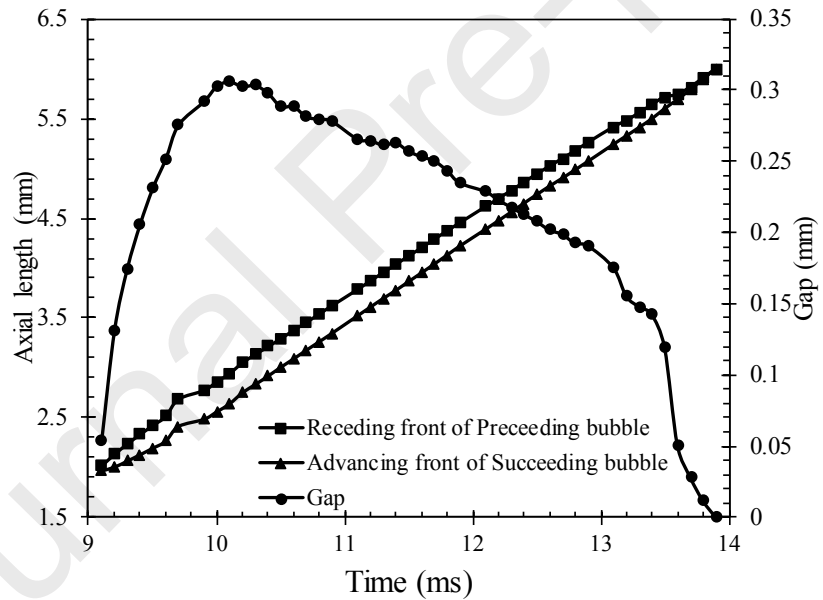
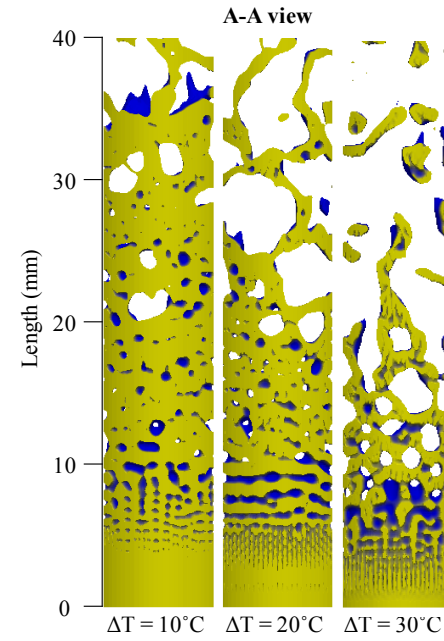
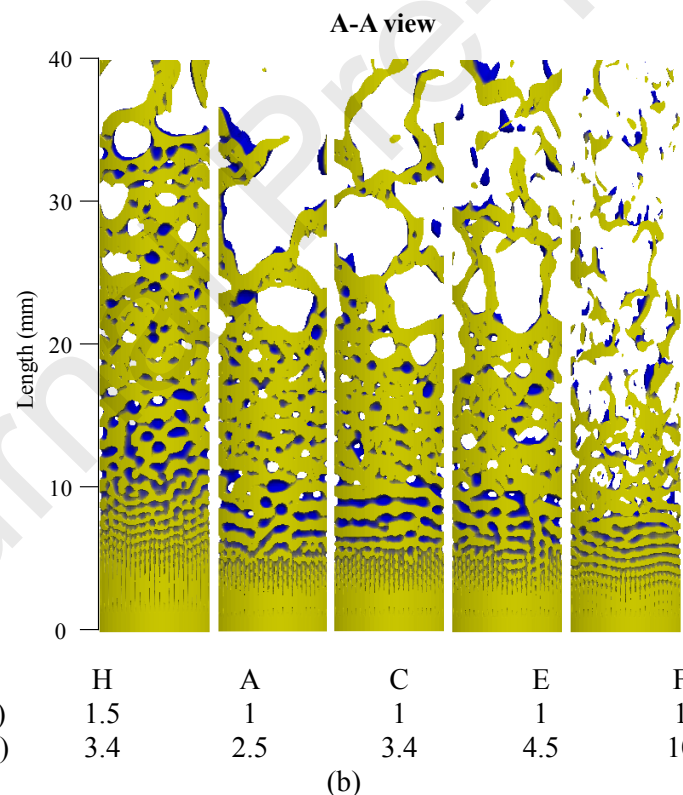


Figure 10: Temporal history of growth and drainage of liquid bridge between neighboring bubbles leading towards merging; advancing and receding fronts of succeeding and preceding bubbles are tracked to determine the gap at a particular time.



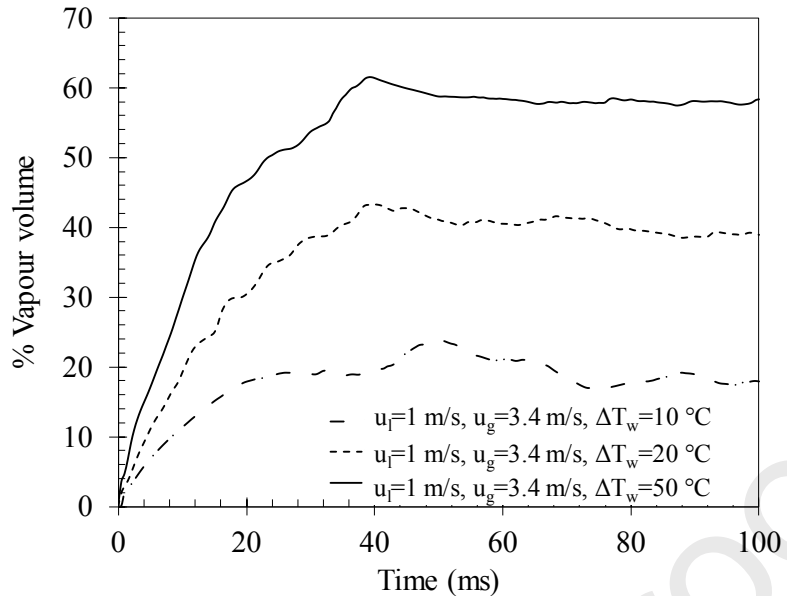
Case	B	C	D
ΔT ($^{\circ}\text{C}$)	10	20	50

(a)

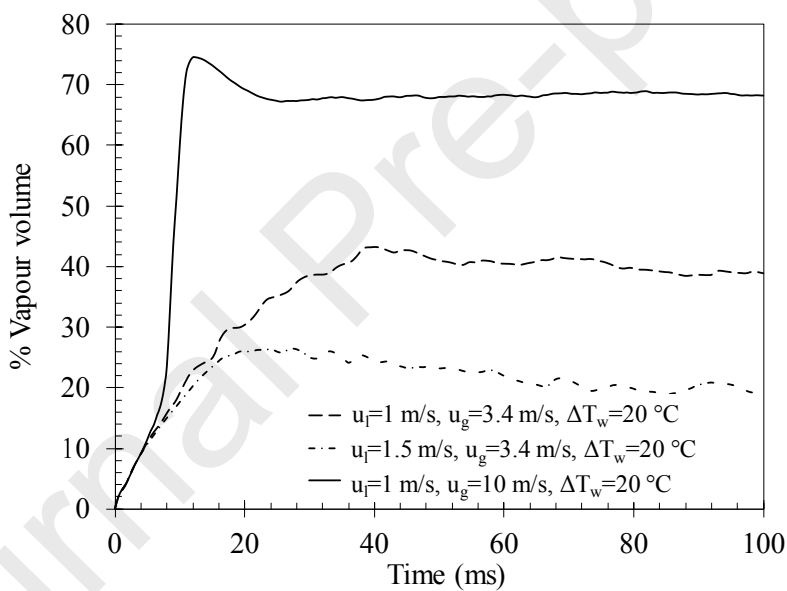


(b)

Figure 11: Comparison of liquid film evolution and dry out length (a) for different degree of superheats and (b) for different flow conditions



(a)



(b)

Figure 12: Plot of % vapor volume generated vs time (a) for different degrees of wall superheat (b) for different vapor velocities

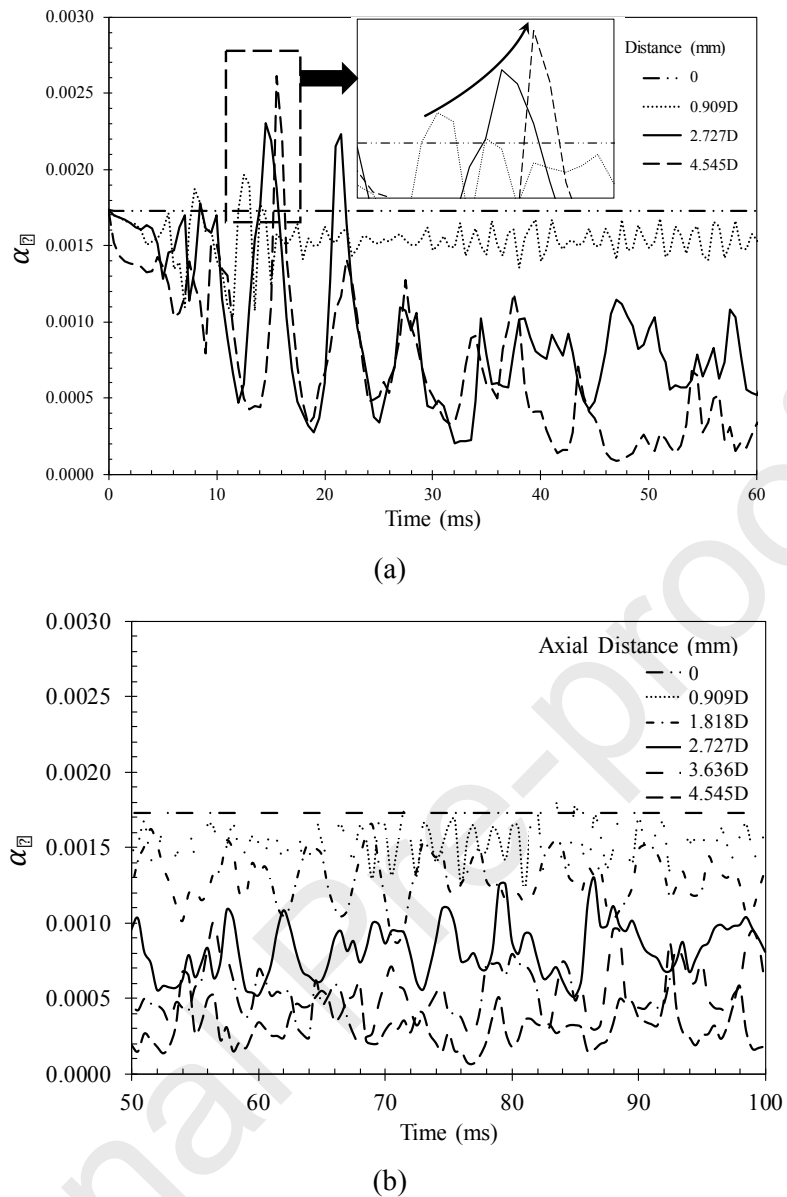


Figure 13: Fluctuation of liquid phase fraction with time at different cross-sections (a) Passage of disturbance wave in the axial direction and its effect on liquid volume fraction in cross-sectional planes. (b) Account of steady-state fluctuations in liquid phase fraction due to life-cycle of a bubble generated in phase change.

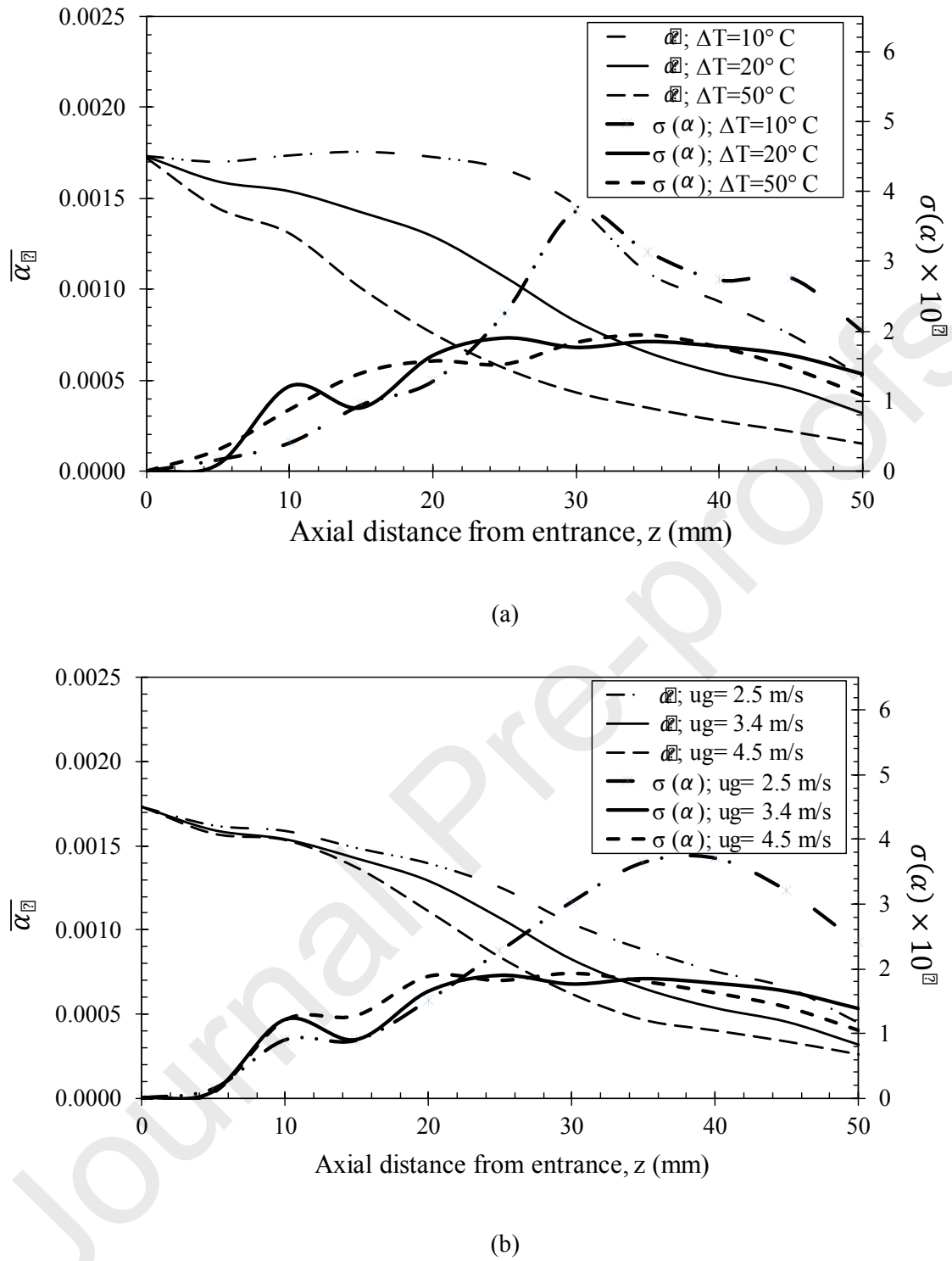


Figure 14: Variation of mean and standard deviation of liquid phase fraction over the length of the pipe (a) for different degrees of superheat (b) for different vapor flow rates

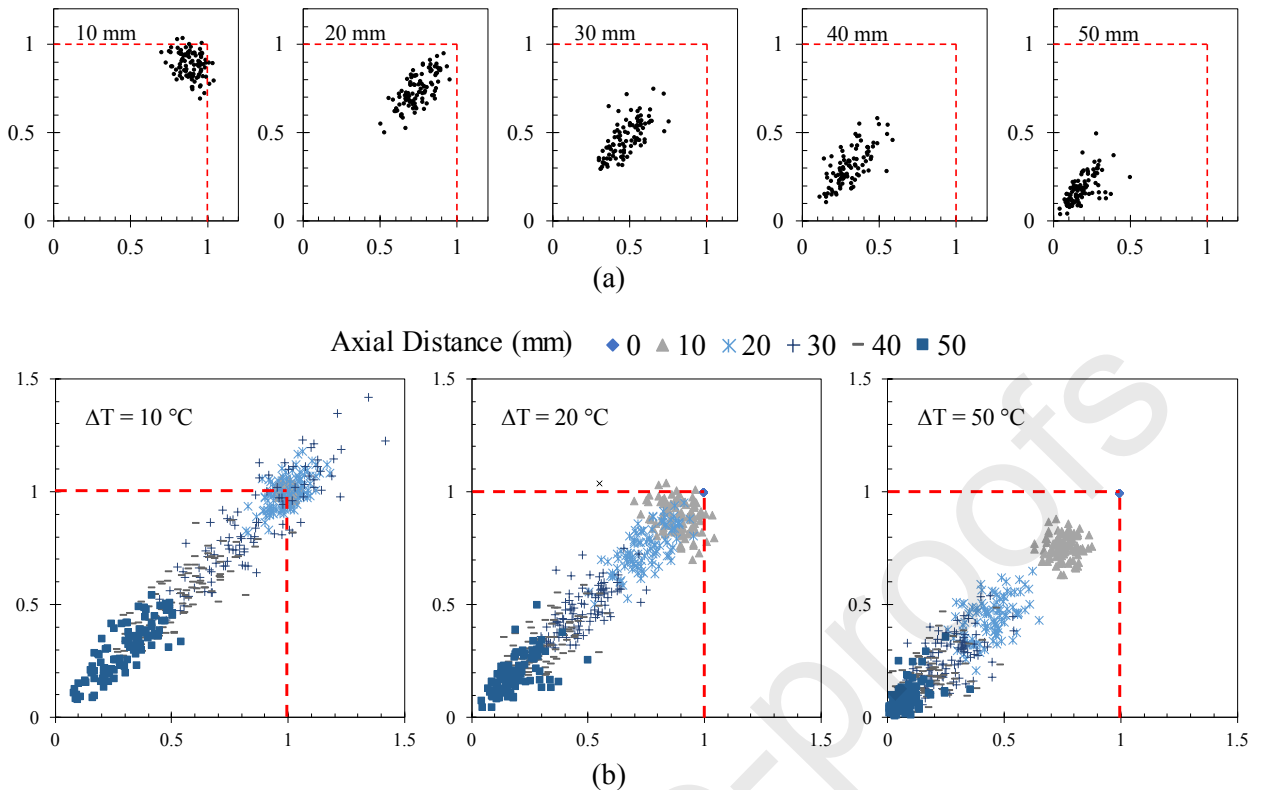


Figure 15: Attractor plot of non-dimensionalised liquid phase fraction (a) at different cross sections for 20°C superheat; Case C (b) at different degrees of superheats; Case B, C & D

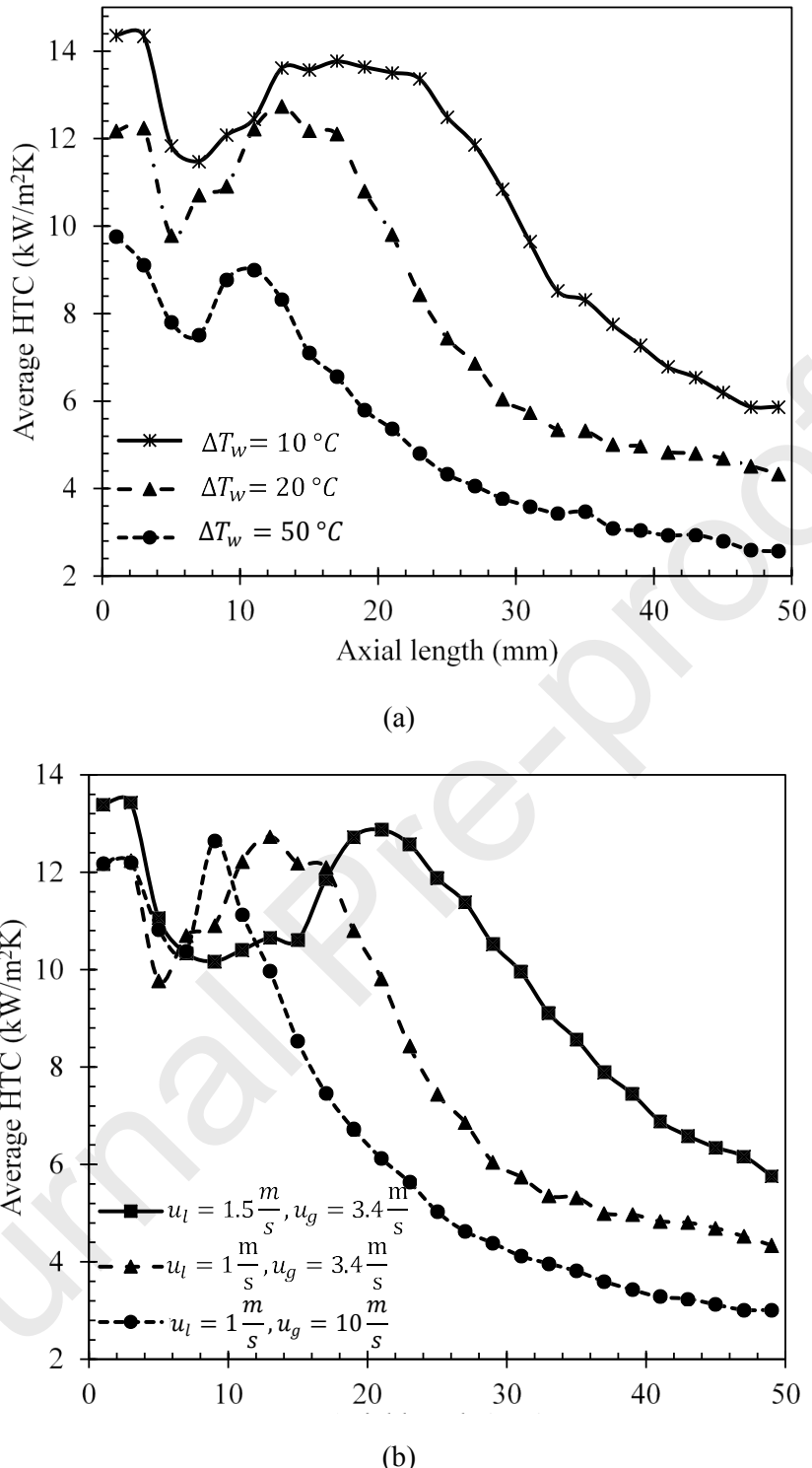


Figure 16: Variation of heat transfer coefficient against axial distance (a) for different degree of superheat (b) for different liquid and vapor velocity

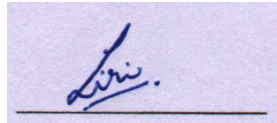
Highlights

- Description of interface evolution on route to dryout in annular flow
- Nucleation, roll wave formation and bubble bursting are shown
- Portrayal of liquid phase fluctuation with attractor plot
- Axial heat transfer coefficient comparison for different flow and superheat

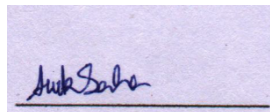
Journal Pre-proofs

Declaration of interest/Conflict of interest

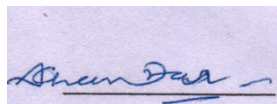
The authors declare that they have no known competing financial interests or personal relationships that could have appeared to influence the work reported in this paper.



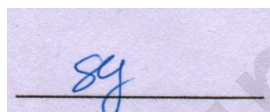
Liril D. Silvi
Department of chemical Engineering,
Indian Institute of Technology, Roorkee, India



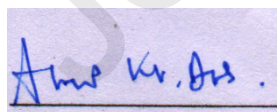
Avik saha,
Department of Mechanical and Industrial Engineering,
Indian Institute of Technology, Roorkee, India



Dinesh K. Chandraker
Reactor Engineering Division,
Bhabha Atomic Research Centre, Mumbai, India



Sumana Ghosh
Department of chemical Engineering,
Indian Institute of Technology, Roorkee, India



Arup Kumar Das
Department of Mechanical and Industrial Engineering,
Indian Institute of Technology, Roorkee, India